The Astronomical Journal, 170:109 (16pp), 2025 August https://doi.org/10.3847/1538-3881/ade677

The Compositions of Rocky Planets in Close-in Orbits Tend to Be Earth-like

Casey L. Brinkman[1,2,30], Lauren M. Weiss[3], Daniel Huber[1,4], Rena A. Lee[1,30], Jared Kolecki[3], Gwyneth Tenn[5], Jingwen Zhang[1,31], Suchitra Narayanan[1,30], Alex S. Polanski[6,7], Fei Dai[1], Jacob L. Bean[8], Corey Beard[9,31], Madison Brady[8], Max Brodheim[10], Matt Brown[10], Ashley Chontos[11], William Deich[12], Jerry Edelstein[13], Benjamin J. Fulton[14], Steven Giacalone[14], Steven R. Gibson[15], Gregory J. Gilbert[16], Samuel Halverson[17], Luke Handley[16,14], Grant M. Hill[10], Rae Holcomb[9], Bradford Holden[12], Aaron Householder[18,19], Andrew W. Howard[14], Howard Isaacson[20], Stephen Kaye[15], Russ R. Laher[21], Kyle Lanclos[10], J. M. Joel Ong[1,32], Joel Payne[10], Erik A. Petigura[16], Daria Pidhorodetska[22], Claire Poppett[13], Arpita Roy[23], Ryan Rubenzahl[14], Nicholas Saunders[1,30], Christian Schwab[24], Andreas Seifahrt[8], Abby P. Shaum[14], Martin M. Sirk[13], Chris Smith[13], Roger Smith[15], Guðmundur Stefánsson[25], Julian Stürmer[26], Jim Thorne[10], Emma V. Turtelboom[20], Dakotah Tyler[27], John Valliant[10], Judah Van Zandt[16], Josh Walawender[10], Samuel W. Yee[28], Sherry Yeh[10], and Jon Zink[14]

[1] Institute for Astronomy, University of Hawai'i, 2680 Woodlawn Drive, Honolulu, HI 96822, USA; clbrinkm@hawaii.edu
[2] McGill University, Trottier Space Institute, 3550 rue University, Montreal, QC H3A 2A7, Canada
[3] Department of Physics and Astronomy, University of Notre Dame, Notre Dame, IN 46556, USA
[4] Sydney Institute for Astronomy (SIfA), School of Physics, University of Sydney, NSW 2006, Australia
[5] Punahou School, 1601 Punahou Street, Honolulu, HI 96822, USA
[6] Department of Physics and Astronomy, University of Kansas, Lawrence, KS 66045, USA
[7] Lowell Observatory, 1400 W Mars Hill Road, Flagstaff, AZ, USA 86001, USA
[8] Department of Astronomy & Astrophysics, University of Chicago, 5640 S. Ellis Avenue, Chicago, IL 60637, USA
[9] Department of Physics & Astronomy, University of California Irvine, Irvine, CA 92697, USA
[10] W. M. Keck Observatory, 65-1120 Mamalahoa Highway, Kamuela, HI 96743, USA
[11] Department of Astrophysical Sciences, Princeton University, 4 Ivy Lane, Princeton, NJ 08544, USA
[12] UC Observatories, University of California, Santa Cruz, CA 95064, USA
[13] Space Sciences Laboratory, University of California, Berkeley, CA 94720, USA
[14] Department of Astronomy, California Institute of Technology, Pasadena, CA 91125, USA
[15] Caltech Optical Observatories, California Institute of Technology, Pasadena, CA 91125, USA
[16] Department of Physics & Astronomy, University of California Los Angeles, Los Angeles, CA 90095, USA
[17] Jet Propulsion Laboratory, California Institute of Technology, 4800 Oak Grove Drive, Pasadena, CA 91109, USA
[18] Department of Earth, Atmospheric, and Planetary Sciences, Massachusetts Institute of Technology, Cambridge, MA 02139, USA
[19] Kavli Institute for Astrophysics and Space Research, Massachusetts Institute of Technology, Cambridge, MA 02139, USA
[20] Department of Astronomy, 501 Campbell Hall, University of California, Berkeley, CA 94720, USA
[21] NASA Exoplanet Science Institute/Caltech-IPAC, MC 100-22, 1200 E. California Boulevard, Pasadena, CA 91125, USA
[22] Department of Earth and Planetary Sciences, University of California, Riverside, CA 92521, USA
[23] Astrophysics & Space Institute, Schmidt Sciences, New York, NY 10011, USA
[24] School of Mathematical and Physical Sciences, Macquarie University, Balaclava Road, North Ryde, NSW 2109, Australia
[25] Anton Pannekoek Institute for Astronomy, University of Amsterdam, Science Park 904, 1098 XH Amsterdam, The Netherlands
[26] Landessternwarte, Zentrum für Astronomie der Universität Heidelberg, Königstuhl 12, D-69117 Heidelberg, Germany
[27] Department of Physics and Astronomy, University of California, Los Angeles, CA 90095, USA
[28] Center for Astrophysics | Harvard & Smithsonian, 60 Garden Street, Cambridge, MA 02138, USA[29]
Received 2024 September 30; revised 2025 June 3; accepted 2025 June 17; published 2025 July 23

Abstract

Hundreds of exoplanets between 1 and 1.8 times the size of Earth have been discovered on close-in orbits. However, these planets show such a diversity in densities that some appear to be made entirely of iron, while others appear to host gaseous envelopes. To test this diversity in composition, we update the masses of five rocky exoplanets (HD 93963 A b, Kepler-10 b, Kepler-100 b, Kepler-407 b, and TOI-1444 b) and present the confirmation of a new planet (TOI-1011) using 187 high-precision radial velocities from Gemini/MAROON-X and Keck/KPF. Our updated planet masses suggest compositions closer to that of Earth than previous literature values for all planets in our sample. In particular, we report that two previously identified "super-Mercuries" (Kepler-100 b and HD 93963 A b) have lower masses that suggest less iron-rich compositions. We then compare the ratio of iron to rock-building species with the abundance ratios of those elements in their host stars. These updated planet compositions do not suggest a steep relationship between planet and host star compositions, contradictory to previous results, and suggest that planets and host stars have similar abundance ratios.

Unified Astronomy Thesaurus concepts: Exoplanets (498); Exoplanet astronomy (486); Super Earths (1655); Extrasolar rocky planets (511); Radial velocity (1332)

1. Introduction

In our effort to contextualize the properties of Earth among the thousands of extrasolar planets discovered, one of the most challenging properties to compare is planet composition.

[29] Heising-Simons Foundation 51 Pegasi b Postdoctoral Fellow.
[30] NSF Graduate Research Fellow.
[31] NASA FINESST Fellow.
[32] NASA Hubble Fellow.

Rocky planet compositions affect habitability (V. Meadows & NAI-Virtual Planetary Laboratory Team 2014; P. E. Driscoll 2018; R. K. Kopparapu et al. 2020) and can inform planet formation scenarios (J. Scora et al. 2020; V. Adibekyan et al. 2021; C. L. Brinkman et al. 2024). To characterize a planet's composition and determine whether it is Earth-like, is iron-rich like Mercury, or hosts a thick atmosphere unlike any small planets in our solar system, we need precisely measured masses and radii. Radial velocity (RV) measurements of transiting planets are one of the best tools to better understand the masses, densities, and compositions of other worlds.

Our ability to determine the composition of small planets from mass and radius measurements is based on an assumption of a purely "rocky" composition. If a planet hosts a water layer or volatile envelope, it becomes impossible to constrain the relative fraction of iron core to rocky mantle for a planet, even with a precisely measured bulk density (D. Valencia et al. 2007; L. A. Rogers & S. Seager 2010). However, for planets that are sufficiently small ($R < 1.5\ R_\oplus$), orbit very close to their host star ($P < 30$ days), and receive large stellar flux, we can assume that they are unlikely to have significant atmospheres (J. E. Owen & Y. Wu 2017) or water/ice layers (E. D. Lopez 2017), due to photoevaporation. This leaves silicate rock and iron as the two primary components of short-period super-Earths. To first order, we can express the composition of rocky planets using the fraction of the planet's mass that is iron, or its core mass fraction (CMF).

The masses and radii of small exoplanets suggest a transition between primarily rocky (super-Earth) and gas-enveloped (sub-Neptune) planets at approximately $1.5\ R_\oplus$ (L. M. Weiss & G. W. Marcy 2014; L. A. Rogers 2015; B. J. Fulton et al. 2017), with planets smaller than $1.5\ R_\oplus$ often having compositions consistent with Earth-like iron-to-silicate ratios (C. D. Dressing et al. 2015). The mass and radius measurements for super-Earths, however, indicate a wide diversity of densities among these planets—far more diverse than we observe for small planets in our own solar system (G. W. Marcy et al. 2014; T. D. Morton et al. 2016; F. Dai et al. 2019). These densities suggest that the interior compositions of Earth and super-Earth-sized planets could potentially vary from entirely made of silicate rock to predominantly made of iron (A. S. Bonomo et al. 2019), with high molecular mass atmospheres possible (I. Angelo & R. Hu 2017; E. S. Kite & L. Schaefer 2021).

To better understand the compositions of rocky worlds, we can place these planets in the context of their host star. Planets are born from the same primordial nebular material as their host star, and it is intuitive to assume that the relative chemical abundances of iron and rock-building elements between star and planet would be similar. While some studies have explicitly assumed similar elemental abundance ratios for stars and planets (C. Dorn et al. 2015), others have tried to test it (M. Plotnykov & D. Valencia 2020; V. Adibekyan et al. 2021; J. G. Schulze et al. 2021; C. L. Brinkman et al. 2024). Most studies found that the uncertainties—especially in mass—are too large in most cases to draw definitive conclusions about the compositions of individual rocky planet and host star systems (M. Plotnykov & D. Valencia 2020; J. G. Schulze et al. 2021). Additionally, many of the best-characterized rocky planets (such as the TRAPPIST-1 system) orbit stars too cool for individual abundance measurements of Fe and Mg.

This apparent diversity of compositions is based on a small sample of rocky planets, with most having large uncertainties on their mass measurements. Rocky planets have small radii and low masses, which are inherently more difficult to measure, and only a handful have masses and radii measured to within 10% (M. Gillon et al. 2017; F. Dai et al. 2019; N. Espinoza et al. 2020; E. Agol et al. 2021; L. Delrez et al. 2021; M. G. Soto et al. 2021; T. Trifonov et al. 2021; A. S. Bonomo et al. 2023; C. L. Brinkman et al. 2023b). Many of the planets that appear to have compositions most dissimilar to Earth, such as high-density "super-Mercuries," have large uncertainties in their mass measurements. Updating these masses with high-precision and high-cadence RV measurements will help to characterize the compositions of these worlds.

To address these issues and better understand the compositional diversity of rocky planets, we report 187 high-precision RVs for six rocky planets, including confirmation of a previously unconfirmed planet TOI-1011 b. We homogeneously update the stellar masses and radii using isochrones and report updated masses and radii for each planet. We then compute the CMF and, where possible, analyze the composition of each planet in relation to that of its host star.

2. Sample Selection

To select targets for our RV survey, we use both objective and subjective criteria to sample a wide variety of apparent compositions. First, we selected planets between 1 and $1.8\ R_\oplus$ that have published RVs using the NASA Exoplanet Archive (queried 4/18/2024; R. L. Akeson et al. 2013), with either a published value for the mass or an upper limit.

We then selected only short-period ($P < 10$ days) and ultra −short-period ($P < 1$ day) planets, because MAROON-X and the Keck Planet Finder (KPF) are both recently commissioned instruments whose long-term stability is still being characterized. As such, our data acquisition strategy was to collect all of our RVs on a particular star within one run on MAROON-X (order of 1 week) and as many as possible per night with KPF. To mitigate long-term stability issues, we use a different vertical offset for each run of MAROON-X data and each night of KPF data (colloquially called the "Floating Chunk" method).

Another large consideration in selecting the sample of planets was available telescope resources. We wanted to produce a sample of planets with masses measured with a fractional precision of 10%, so we selected planets that could meet this threshold with the number of RVs we are able to collect over three years of observing. To determine this, we simulated RV measurements with fractional uncertainties of $1\ \mathrm{m\,s^{-1}}$ to mimic those collected by MAROON-X and KPF, and we added those to the existing RV data sets for a particular star and recovered the best-fit semiamplitude and 1σ uncertainty. We then determined how many RVs would be necessary to measure a semiamplitude for the planet to 10% uncertainty (using the previously published semiamplitude) and then calculated the necessary exposure time to achieve $1\ \mathrm{m\,s^{-1}}$ precision on that star with either MAROON-X or KPF.

We selected nine planets for our survey that meet these criteria and represent planets that range from low-density planets likely to host gaseous envelopes, to Earth-like planets, to high-density super-Mercuries: Kepler-10 b, Kepler-100 b,

Kepler-407 b, Kepler-93 b, Kepler-99 b, TOI-561 b, TOI-1444, HD 93963 A b, and GJ 3929 b. The RV analysis for TOI-561 b was presented separately in C. L. Brinkman et al. (2023b). For three of these planets (Kepler-93 b, Kepler-99 b, and GJ 3929 b) the KPF RVs are still preliminary and will be published at a later date when the wavelength solution is stable enough that a night-to-night offset is not needed.

We include one additional unconfirmed planet in our sample: TOI-1011. This planet was discovered as part of a search for RV signals in archival HARPS-N RVs around stars flagged with planet candidates from TESS. Because the radius, preliminary mass measurement, and orbital period from this were consistent with our survey criteria, we added TOI-1011 to our sample.

3. Observations

3.1. HIRES

Our analysis incorporates RVs from the High Resolution Echelle Spectrograph (HIRES) on the W. M. Keck Observatory 10 m telescope Keck I on Maunakea, Hawai'i (S. S. Vogt et al. 1994). We observed TOI-561, Kepler-10, Kepler-100, and Kepler-407 with HIRES from 2021 February to 2023 January.[33] HIRES is a well-characterized spectrograph, with demonstrated stability (A. W. Howard et al. 2010).

We used the standard California Planet Search (CPS) data reduction pipeline as described in A. W. Howard et al. (2010). This method uses an iodine cell mounted in front of the slit in order to provide a provide a wavelength reference (G. W. Marcy & R. P. Butler 1992). Sky subtraction was performed as part of the raw reduction through the use of a 14.″0-long slit in order to spatially resolve the sky with respect to the seeing-limited point-spread function (FWHM $\approx$ 1.″0). Measuring the RVs requires characterizing the PSF of the spectrometer, which is time-variable owing primarily to changing seeing and weather. The CPS Doppler routine involves forward-modeling the iodine-imprinted spectrum of a star as the combination of a library iodine spectrum and a velocity-shifted, iodine-free, PSF-deconvolved template spectrum of the target star, the combination of which is then convolved with the best-fit PSF. To deconvolve the PSF from the iodine-free template, we observed rapidly rotating B stars with the iodine cell in the light path immediately before and after the template, effectively sampling the PSF at the time of the template in the iodine absorption profiles.

3.2. MAROON-X

MAROON-X is a new fiber-fed spectrograph mounted on the 8.1 m Gemini-North telescope on Maunakea, Hawai'i. It operates in the red–optical (500–920 nm) with resolving power $R \approx 85{,}000$ and uses both red and blue arms to get two RV measurements per exposure (A. Seifahrt et al. 2016, 2018, 2020). MAROON-X has demonstrated an intra-night stability of 30 cm s^{-1} and has been used to measure some of the most precise masses for rocky planets in the literature to date (T. Trifonov et al. 2021; J. G. Winters et al. 2022; C. L. Brinkman et al. 2023b). We observed TOI-561, TOI-1011, Kepler-10, Kepler-100, and Kepler-407 with MAROON-X between 2021 January and 2023 December.

Our observations used the simultaneous calibration fiber of MAROON-X, which allows for a robust order-by-order drift correction to sub-meter-per-second precision. The raw data were reduced using a custom pipeline based on CRIRES (J. Bean et al. 2010), and RVs were computed using `SERVAL` (M. Zechmeister et al. 2018). A full description of MAROON-X data reduction can be found in J. G. Winters et al. (2022).

Exposure times were chosen to achieve a precision of 1 m s^{-1} on our RVs for most targets (and 1.5 m s^{-1} on Kepler-407 owing to large integration times). We estimated the necessary exposure time by scaling the demonstrated RV precision from 51 Pegasi (21 cm s^{-1} photon-limited precision for a 120 s exposure) using $\frac{\sigma_{\rm RV}}{\sigma_{\rm RV0}} = \frac{\rm SNR_0}{\rm SNR} = \sqrt{\frac{F_0 \times t_0}{F \times t}}$. Most of our targets were similar spectral types to 51 Pegasi (G type), and we found strong agreement between our estimated and actual RV precision.

3.3. KPF

KPF (S. R. Gibson et al. 2024) is a fiber-fed spectrograph that observes in the optical regime with a wavelength coverage of 445–870 nm and a resolving power of $R \approx 95{,}000$. This wavelength range is broken into a green channel (445–600 nm) and a red channel (600–870 nm). Additionally, a UV spectrometer (385–405 nm) monitors Ca II H and K, the emission cores of which are commonly used as indicators for magnetic activity in the stellar chromosphere. With a goal of Doppler precision of 30 cm s^{-1}, KPF is exceptionally well suited to measure the small semiamplitudes of rocky planets (F. Dai et al. 2024).

We obtained spectra of Kepler-10, Kepler-100, TOI-1444, and HD 93963 with KPF across 2023A and 2023B (2023 May–2024 January). We used the publicly available exposure time calculator[34] to estimate the exposure time necessary to produce RVs with 1 m s^{-1} precision. The spectra were reduced with the KPF Data Reduction Pipeline (DRP), also available on Github.[35]

The wavelength calibration for KPF includes Th-Ar and U-Ne lamps, a Laser Frequency Comb, a Fabry–Pérot Etalon, and the Solar Calibrator (R. A. Rubenzahl et al. 2023). Wavelength calibration of KPF DRP is still in development at the time of writing, and nightly offsets in the wavelengths are anticipated. To mitigate this effect, we give each night of KPF data a different vertical offset (γ) in the RV model. As such, only KPF nights with high-cadence observations for each star are useful, although we anticipate that future work on the wavelength solution will allow comparison of RVs across multiple nights.

3.4. HARPS-North

Our analysis of Kepler-10 and TOI-1011 also incorporates published RVs from the HARPS-N spectrograph installed on the 3.6 m Telescopio Nazionale Galileo at the Observatorio Roque de Los Muchachos in La Palma, Spain. These RVs are taken from A. S. Bonomo et al. (2023).

[33] Telescope time was allocated by University of Hawaii.

[34] https://github.com/California-Planet-Search/KPF-etc

[35] https://github.com/Keck-DataReductionPipelines/KPF-Pipeline

4. Methodology

4.1. RV Fitting and Planet Masses

We used the open-source Python package `RadVel` (B. J. Fulton et al. 2018) to model the RVs. We measured the mass of each planet by modeling the RVs for a Keplerian orbit, in which the RV curve is described by the orbital period (P), inferior conjunction time (T_c), eccentricity (e), argument of periastron, and RV semiamplitude (K) of each planet. In all instances we used the orbital period and conjunction time—along with their uncertainties—from the photometric transit fit as Gaussian priors on these parameters. For most planets we assumed circular orbits (K. M. Deck et al. 2013; S. M. Mills et al. 2019; V. Van Eylen et al. 2019; S. W. Yee et al. 2021) and checked that this was consistent with previous literature fits. We then allowed eccentricity to vary and found in all instances that the resulting RV fit was consistent with a fixed zero eccentricity. We did not use priors for semiamplitude.

We included two additional terms per data set to fit the RVs: a zero-point offset (γ) and an RV jitter term (σ_j). Jitter accounts for additional Gaussian noise that can be astrophysical in origin, or it can come from systematics of the spectrograph. This additional uncertainty was added in quadrature with the intrinsic uncertainties on the RVs during our optimization of the likelihood function and Markov Chain Monte Carlo (MCMC) analysis. The likelihood function used in `RadVel` is

$$\ln(\mathcal{L}) = -\sum_i \frac{(v_i - v_m(t_i))^2}{2(\sigma_i^2 + \sigma_{\rm jit}^2)} - \ln\sqrt{2\pi(\sigma_i^2 + \sigma_{\rm jit}^2)}, \quad (1)$$

where $\mathcal{L}$ is the likelihood, v_i and σ_i are the ith RV measurement and its associated uncertainty, $v_m(t_i)$ is the Keplerian model RV at time t_i, and $\sigma_{\rm jit}$ is the jitter estimate. We used initial guesses of 1 m s^{-1} for σ_j and 0 for γ, with no constraining priors. After optimizing for the maximum likelihood fit, we ran `RadVel`'s built-in MCMC algorithm (D. Foreman-Mackey et al. 2013) to estimate the uncertainty in the model parameters and to explore the covariance between parameters.

Once we found the best-fit RV model for each system, we calculated the planet mass (m) using the best-fit semiamplitude (K), orbital period (P), inclination (i), eccentricity (e), and stellar mass (M) using the following relation (C. Lovis & D. Fischer 2010):

$$K = \frac{28.4329}{\sqrt{1-e^2}} \frac{m\sin(i)}{M_J} \left(\frac{m+M}{M_\odot}\right)^{-2/3} \left(\frac{P}{1\ \rm yr}\right)^{-1/3}. \quad (2)$$

We used our updated stellar masses (Table 1), along with literature values for orbital period and inclination for all previously confirmed systems (table insert). We used orbital period and inclination from our photometric analysis for TOI-1011 b.

4.2. Planet Compositions

Using the mass and radius of each planet, we calculated the CMF, a measure of the mass fraction of the iron core to the total planet mass[36] (e.g., S. Seager et al. 2007; A. R. Howe et al. 2014; L. Zeng et al. 2016). This is a measure of the minimum CMF for the planet and is only an accurate CMF in the absence of a volatile envelope or water layer. Because we have selected only short-period and ultra−short-period planets with $R < 1.5\ R_\oplus$, they are less likely to host these low-density components (E. D. Lopez 2017; J. E. Owen & Y. Wu 2017). However, this is not universally true, and there are ultrahot super-Earths likely to host gaseous envelopes, such as TOI-561 b (G. Lacedelli et al. 2021; C. L. Brinkman et al. 2023b).

We used `SuperEarth` (D. Valencia et al. 2006; M. Plotnykov & D. Valencia 2020) to model the interior composition of each planet. The package solves equations of state for iron and rock-building minerals to match the mass and radius values provided. `SuperEarth` first assumes that planets are composed entirely of iron (Fe), magnesium (Mg), silicon (Si), and oxygen (O) and ignores all other trace elements. `SuperEarth` then builds a planet with two primary, differentiated layers: an iron core and a rocky mantle. The mantle is broken down into four components (upper mantle, transition zone, lower mantle, and lower-most mantle) like that of Earth, distinguished by the mineral phase boundaries determined by the pressure and temperature of the mantle. The upper mantle includes olivene ($MgSiO_4$) and pyroxene; the transition zone features wadsleyite, ringwoodite, and pyroxene; the lower mantle includes bridgmanite and magnesiowustite; and the lower-most mantle has the same composition as the lower mantle but features a high-pressure bridgmanite (post-perovskite). The core is subdivided into an inner and outer core following the melting line of iron alloy. A more thorough description of `SuperEarth` can be found in M. Plotnykov & D. Valencia (2020).

Constructing this model involved making several assumptions about the compositions of the mantle and core. For this analysis we assume an Earth-like ratio of Mg/Si = 0.97361 in the mantle, we assume no silica inclusions in the iron core, and we assume an iron mole fraction in the mantle of 0.1 based on expected limits for alloy content in Earth's core (W. F. McDonough & S. Sun 1995). Variations in the iron fraction in the mantle of order 10% produce a change of 0.03 CMF, which is smaller than our CMF uncertainties. For silicate inclusions in the core, however, variations of 10% produce a change of 0.1 in CMF. Allowing the ratio of Mg/Si in the mantle to vary (using the values of their host star as priors) produces differences in CMF of ∼0.02. While these possible variances are small enough to not significantly impact our CMF calculation or our conclusions, we partially account for these potential sources of error using a very conservative approach to measuring CMF uncertainties.

To compute CMF uncertainties, we drew 1000 values for the mass and radius of each planet from Gaussian distributions centered on best-fit values with 1σ error bars. We then propagated these values through `SuperEarth` and took the standard deviation of the resulting CMF distribution (after ensuring that distribution was also Gaussian). We assumed no correlation between planet mass and radius, although there very likely is a strong correlation, and therefore our Monte Carlo draws represent conservative uncertainty estimates.

4.3. Host Star Properties

4.4. Atmospheric Parameters

For most stars in our sample we use literature values for $T_{\rm eff}$, [M/H], [α/Fe], and log(g), but for TOI-1011 we measure our own using a single HARPS-N spectrum obtained on 2019

[36] For reference, Earth is 32.5% iron by mass, giving it a CMF of 0.325.

Table 1
Stellar Parameters

Star Name	Radius ($R_\odot$)	Mass ($M_\odot$)	Luminosity ($L_\odot$)	$T_{\rm eff}$ (K)	log(g)	[Fe/H] (dex)	[Mg/H] (dex)	[α/Fe] (dex)	CMF$_*$
HD 93963 A	1.03 ± 0.01	1.09 ± 0.02	1.19 ± 0.05	5987 ± 64 [S]	4.5 ± 0.1	0.1 ± 0.04	0.08 ± 0.06	⋯	0.31
Kepler-10	1.06 ± 0.06	0.89 ± 0.05	1.1 ± 0.1	5671 ± 100 [P]	4.4 ± 0.1	-0.17 ± 0.04	-0.07 ± 0.05	0.10 ± 0.04	0.25
Kepler-100	1.51 ± 0.05	1.13 ± 0.05	2.48 ± 0.07	5837 ± 100 [P]	4.1 ± 0.1	0.10 ± 0.04	0.05 ± 0.05	-0.02 ± 0.04	0.33
Kepler-407	1.04 ± 0.05	0.99 ± 0.05	0.78 ± 0.05	5487 ± 100 [B]	4.3 ± 0.1	0.35 ± 0.05	0.33 ± 0.07	-0.03 ± 0.04	0.31
TOI-1011	0.92 ± 0.03	0.91 ± 0.03	0.70 ± 0.03	5475 ± 84	4.5 ± 0.05	0.03 ± 0.04	⋯	0.05 ± 0.04	⋯
TOI-1444	0.91 ± 0.03	0.88 ± 0.05	0.63 ± 0.02	5377 ± 100 [P]	4.4 ± 0.1	0.04 ± 0.04	0.04 ± 0.05	0.01 ± 0.04	0.29

Note. Uncertainties on CMF are all 0.03. All stellar masses and radii were measured homogeneously using the $T_{\rm eff}$, [Fe/H], and log(g) listed here. $T_{\rm eff}$, log(g), [Fe/H], and [Mg/H] for HD 93963 A are from L. M. Serrano et al. (2022), those for Kepler-407 are from J. M. Brewer & D. A. Fischer (2018), and those for TOI-1011 are measured here. Kepler-10, Kepler-100, and TOI-1444 have parameters measured from A. Polanski et al. (2025, in preparation) and also found in C. L. Brinkman et al. (2024). Quoted stellar parameters and precisions do not include potential systematic errors from different model grids (J. Tayar et al. 2022).

March 20 ($T_{\rm exp} = 1165$ s, signal-to-noise ratio = 92 at $\lambda = 530$ nm). This was done using the code `moogplusplus`[37] (J. Kolecki et al. 2025, in preparation). $T_{\rm eff}$ and log(g) were calculated by fitting photometry to a grid of MIST isochrones. These parameters are used to interpolate an appropriate model atmosphere from a precalculated grid of PHOENIX atmospheres (T. O. Husser et al. 2013).

`moogplusplus` then fits abundances using line-by-line spectral synthesis, performing a χ^2_ν minimization fit to the observed data for spectral lines of a given element. Perturbing the abundance until the residuals are sufficiently minimized results in a best-fit synthetic spectrum for each observed line feature of a given element. Each individual synthetic spectral line fit has its own unique abundance value, resulting in a distribution of abundance values.

By taking the median of this distribution, we can report a single value for the abundance of the chosen element in the star. With the HARPS-N spectrum of TOI-1011, we were able to successfully fit 388 lines of Fe, resulting in median values of A(Fe) = 7.53 ± 0.03 and [Fe/H] = 0.03 ± 0.01. This uncertainty on [Fe/H] represents the intrinsic uncertainty, and we inflate it to 0.04 dex to account for potential systematic uncertainties, which is the median uncertainty of other [Fe/H] values in our sample and in agreement with G. Torres et al. (2012). `moogplusplus` calculates [α/Fe] as the average of the abundances of Ca and Ti, resulting in a value for TOI-1011 of [α/Fe] = 0.05 ± 0.04.

4.4.1. Masses and Radii

To create a more homogeneously characterized sample of planets, we updated the masses and radii of each host star in our sample using `isoclassify` (D. Huber et al. 2017). We used the "direct mode" to calculate the luminosity of each star using $T_{\rm eff}$, [M/H], and log(g), along with the Gaia DR3 parallax, Two Micron All Sky Survey K-band magnitude, a 3D dust map, and bolometric corrections. We then used these derived luminosities, $T_{\rm eff}$, and [M/H] in the "grid mode" of `isoclassify` to infer the mass and radius of each star from a grid of MIST isochrones (J. Choi et al. 2016). Our newly derived luminosities, masses, and radii of the planet-hosting stars are listed in Table 1 and shown in Figure 1.

[37] https://github.com/kolecki4/moogplusplus

We use literature spectroscopic values for $T_{\rm eff}$, [M/H], and log(g) from Polanski et al. (2025, in preparation; Kepler-10, Kepler-100, TOI-561, and TOI-1444), J. M. Brewer & D. A. Fischer (2018; Kepler-407), and L. M. Serrano et al. (2022; HD 93963 A).

4.4.2. Compositions

To compare the composition of our planets with that of their host star, we must express the stellar abundances and planet compositions in equivalent quantities. For stars with measured iron and magnesium abundances, we computed the mass ratio of Fe/Mg from these abundance measurements and then computed the stellar equivalent value of planet CMF. Stellar abundance measurements are given in the form

$$[\mathrm{E/H}] = \log_{10}\left(\frac{n(\mathrm{E})/n(\mathrm{H})_*}{n(\mathrm{E})/n(\mathrm{H})_\odot}\right), \quad (3)$$

where $n(\mathrm{E})/n(\mathrm{H})_*$ is the number density of an element E relative to hydrogen. To turn this into an absolute number density for the star (not relative to the Sun), we used the number density for each element in the Sun relative to hydrogen, given as

$$A(\mathrm{E}) = 12 + \log_{10}(n(\mathrm{E})/n(\mathrm{H})_\odot). \quad (4)$$

Using $A(\mathrm{Fe}) = 7.46 \pm 0.04$, $A(\mathrm{Mg}) = 7.55 \pm 0.03$, and $A(\mathrm{Si}) = 7.51 \pm 0.03$ (M. Asplund et al. 2021), we solved for the number density of these three elements relative to hydrogen ($n(\mathrm{E})/n(\mathrm{H})_\odot$). We then used these values to solve for $n(\mathrm{E})/n(\mathrm{H})_*$ in Equation (3). With values for the number density of each element, we then calculated the mass of each of these elements relative to hydrogen using the atomic weights of each species (55.85 u for Fe and 24.3 u for Mg). This allows us to calculate the mass ratio Fe/Mg for each star.

For planets, each value of CMF corresponds to a specific mass ratio of iron to magnesium assuming a constant ratio of rock-building species, with Fe/Mg approaching infinity as CMF approaches 1. We can use the 1-to-1 mapping between CMF and Fe/Mg to calculate the expected CMF if a planet shares the same Fe/Mg mass ratio as its host star. To do this, we use `SuperEarth` (namely the `st_pl` function) to translate the measured value of Fe/Mg for each star into an equivalent value for "CMF" that we denote as CMF$_*$.

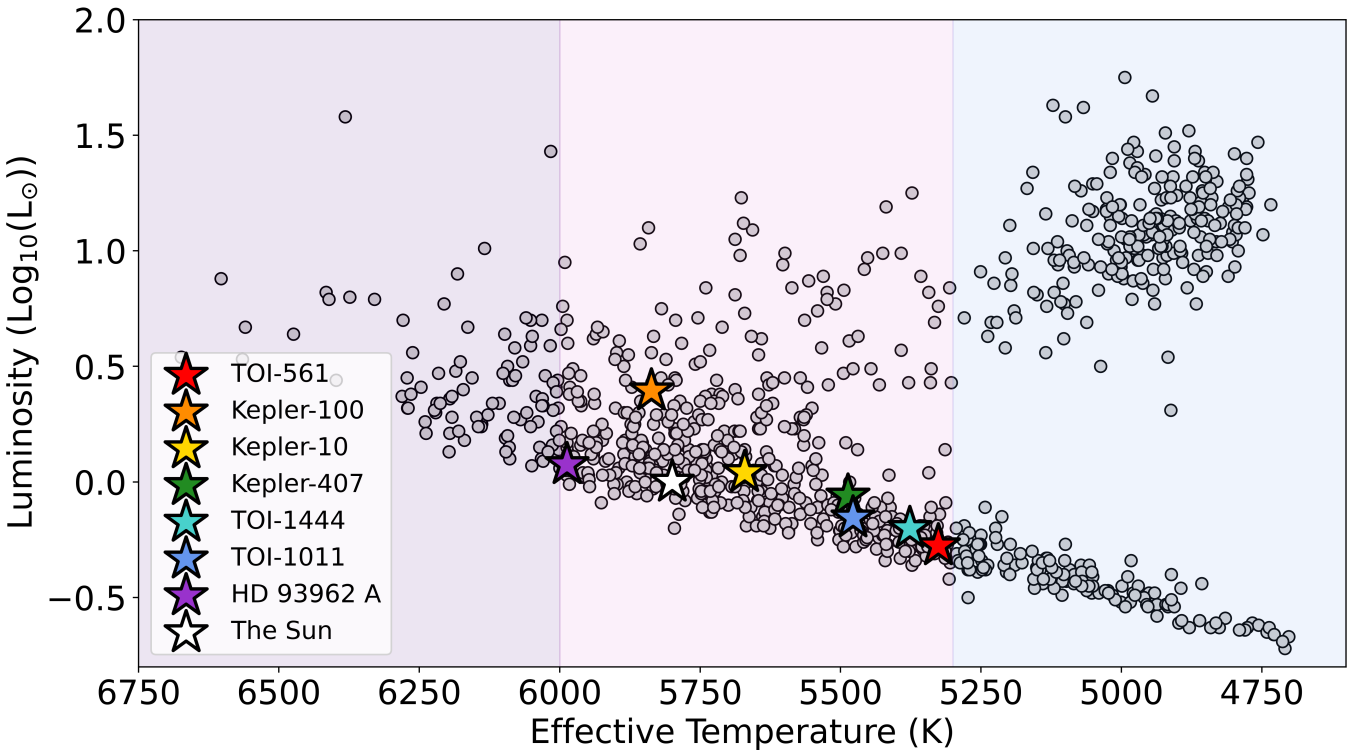

Figure 1. Effective temperature vs. luminosity is shown for all stars in our sample (colored stars), along with a larger sample of exoplanet host stars from the SPOCS catalog (J. M. Brewer & D. A. Fischer 2018). Stars of spectral type G are shown in the pink shaded region (center), those of type F in the purple shaded region (left), and K in the blue shaded region (right).

`SuperEarth` calculates this using the amount of olivine and pyroxene in the mantle (here 0.6), the amount of silica in the iron core (0.0), the amount of iron in the rocky mantle (0.1), and the atomic weight of each species to compute Fe/Mg from CMF. This allows us to compare equivalent quantities for star and planet composition and test the hypothesis that stars and planets share the same chemical ratios.

We calculated the uncertainties in CMF_* by drawing 1000 values of [E/H] from Gaussian distributions centered on our measurements with 1σ widths, then computing the Fe/Mg mass ratio and CMF_* for each draw, and taking the standard deviation of the resulting CMF_* distributions for each star. Despite being calculated independently, the uncertainties on CMF^* are all rounded to 0.03, due to the consistency in [Fe/H] and [Mg/H] uncertainties.

5. Individual Systems

We present the RV analysis and mass measurements for six planets below. We then compute the CMF of each planet and compare to that of their host star where possible. The masses and CMFs for each planet are listed in Table 2. We also include Kepler-102 d (C. L. Brinkman et al. 2023a) in our tables and plots (not part of the 10-planet sample we observed). A list of the host star parameters we used can be found in Table 1.

5.1. Kepler-100 b

Kepler-100 (KOI-41) is a Sun-like star hosting three transiting super-Earth and sub-Neptune-sized planets discovered with Kepler, as well as an additional outer sub-Saturn-sized planet discovered with RVs (L. M. Weiss et al. 2024). The innermost planet (Kepler-100 b) is likely rocky with an orbital period of $P_b = 6.89$ days (P. Gajdoš et al. 2019). Kepler-100 c is likely a gaseous sub-Neptune with a radius of $R_c = 2.35 \pm 0.20\ R_\oplus$ at an orbital period of $P_c = 12.82$ days. [38] Typically, in multiplanet systems with both gaseous and rocky planets we expect the smaller planets to be interior to the larger ones (D. R. Ciardi et al. 2013; E. D. Lopez & J. J. Fortney 2013; L. M. Weiss et al. 2018). However, Kepler-100 d is also likely a rocky planet with a radius of $R_d = 1.6\ \pm 0.2\ R_\oplus$ at an orbital period of $P_d = 35.33$ days.

Previously, both RVs and transit timing variations (TTVs) have been used to measure the masses of the Kepler-100 planets. Initial RV measurements gave only upper limits for planets c and d while giving a very high mass of $M_b = 7.3 \pm 3.2\ M_\oplus$ for planet b (G. W. Marcy et al. 2014), which, combined with the literature radius ($R_b = 1.35 \pm 0.06\ R_\oplus$; T. A. Berger et al. 2018), suggests an extremely iron-rich planet with a $\mathrm{CMF}_b = 0.97$. Y. Judkovsky et al. (2022) use TTVs to measure masses for all three transiting planets, demonstrating the gaseous nature of planet c ($M_c = 14.6 \pm 2.8\ M_\oplus$) and giving a surprisingly low mass for planet d ($M_d = 1.1 \pm 0.5\ \ M_\oplus$, $\mathrm{CMF}_d = -0.9$). Most recently, L. M. Weiss et al. (2024) measured RV masses for planets b ($M_b = 5.5 \pm 1.3\ M_\oplus$) and c ($M_c = 3.8 \pm 1.7\ M_\oplus$) and only measured a mass upper limit for planet d. This mass for planet b still suggests an extremely high iron content with a CMF_b of 0.8, indicating that this might be an iron-enriched super-Mercury planet.

[38] The citations on the planet radii and periods on planets c and d are the same as for planet b.

Table 2
Planet Radius and Mass Are Calculated Using R_p/R_* and Semiamplitude Listed Here and Stellar Parameters from Table 1

Planet Name	Orbital Period (Days)	R_p/R_*	Planet Radius ($R_\oplus$)	Semiamplitude ($m\ s^{-1}$)	Planet Mass ($M_\oplus$)	Core Mass Fraction
HD 93963 A b	1.037611(9)	0.0131 ± 0.0006 [P]	1.49 ± 0.04	2.56 ± 0.99	4.31 ± 1.66	0.33 ± 0.42
Kepler-10 b	0.8374907(2)	0.01268 ± 0.00004 [D]	1.47 ± 0.03	2.58 ± 0.24	3.58 ± 0.33	0.16 ± 0.20
Kepler-100 b	6.88734(7)	0.008062 ± 0.001 [M]	1.34 ± 0.12	1.25 ± 0.15	4.01 ± 0.47	0.59 ± 0.30
Kepler-407 b	0.6693124(6)	0.010404 ± 0.0002 [M]	1.19 ± 0.05	1.41 ± 0.39	1.93 ± 0.50	0.35 ± 0.32
TOI-1011 b	2.470498(7)	0.0143 ± 0.0006	1.45 ± 0.05	2.03 ± 0.30	4.04 ± 0.59	0.33 ± 0.19
TOI-1444 b	0.470269(4)	0.01427 ± 0.0004 [P]	1.42 ± 0.04	2.85 ± 0.37	3.34 ± 0.43	0.22 ± 0.17

Note. Semiamplitudes are measured in this work along with the R_p/R_* for TOI-1011. Citations for literature R_p/R_* values are as follows: D = F. Dai et al. (2021); M = T. D. Morton et al. (2016); P = A. S. Polanski et al. (2024). The value in parentheses following the last digit on Orbital Period represents the uncertainty on the last digit (example: 1.037611(9) is the same as 1.037611 ± 0.000009).

We collected 31 RVs on this system with MAROON-X over three semesters, and we collected eight RVs using HIRES. In addition, we utilized archival HIRES RVs from L. M. Weiss et al. (2024).

We fit the four known planets in the system, assuming zero-eccentricity orbits for the three transiting planets, as is typical for compact multiplanet systems (K. M. Deck et al. 2013; S. M. Mills et al. 2019; V. Van Eylen et al. 2019; S. W. Yee et al. 2021). We then confirmed that fixing $e = 0$ provided a superior fit by comparing the Bayesian Information Criterion of our preferred model to one with nonzero eccentricities. We allowed the eccentricity of the outer giant to vary, with a Gaussian prior centered on an eccentricity of 0.03 with a width of 0.1 (L. M. Weiss et al. 2024).

We measured a semiamplitude of $K_b = 1.25 \pm 0.15\ m\ s^{-1}$, which translates to a planet mass of $M_b = 3.94 \pm 0.47\ M_\oplus$ using the updated stellar mass. With our homogeneously measured stellar radius and R_p/R_* from T. D. Morton et al. (2016), we measure an updated radius of $R_b = 1.34 \pm 0.12\ R_\oplus$. Combining mass and radius measurements, we calculated a CMF of $CMF_b = 0.59 \pm 0.30$. The 1σ upper bound on CMF suggests that Kepler-100 b could potentially be an iron-rich super-Mercury, but our mass suggests that the planet is lower in density than previously determined and has a CMF consistent with that suggested by its host star ($CMF_* = 0.33$) to within 1σ.

5.2. Kepler-10 b

Kepler-10 (KOI 72) b was the first rocky planet discovered by the Kepler mission (N. M. Batalha et al. 2011). It is an ultra−short-period planet orbiting its host every 0.84 days. Kepler-10 also hosts two outer companions: a $P_c = 45.45$-day sub-Neptune-sized transiting planet, and a nontransiting planet with a period of $P_d = 151.0$ days and a minimum mass of $M\sin(i) = 12.68\ M_\oplus$ (A. S. Bonomo et al. 2023). There is also structure in the periodogram of the RV residuals with power at $P = 25$ days, potentially suggestive of a planet candidate at this period (L. M. Weiss et al. 2024), although this has previously been attributed to a harmonic of the rotational period of the star (V. Rajpaul et al. 2017).

As a chemically and dynamically confirmed thick-disk star (X. Dumusque et al. 2014), Kepler-10 has lower metallicity (-0.17 ± 0.04) and an [Fe/Mg] ratio consistent with a CMF_* of 0.25 (C. L. Brinkman et al. 2024). As such, constraining the interior composition of Kepler-10 b would be very helpful to understand both the relationship between planet and host star and the compositions of old rocky planets around thick-disk stars. Recent RV surveys from L. M. Weiss et al. (2024) and A. S. Bonomo et al. (2023) measure a mass of $3.7 \pm 0.4\ M_\oplus$ and $3.26 \pm 0.3\ M_\oplus$, respectively, suggestive of an Earth-like density but a lower $CMF_b \approx 0.15$.

To improve on this measurement, we collected nine RVs with MAROON-X in 2021B, with 10 simultaneous RVs from HIRES. We also obtained 15 RVs with KPF in 2023A. In addition, we utilized the 79 previously collected HIRES RVs (L. M. Weiss et al. 2016, 2024), as well as 291 RVs from HARPS-N (A. S. Bonomo et al. 2023).

We fit for the three planets in the system using a simple Keplerian fit for our full data set. We report a value of $K_b = 2.57 \pm 0.24\ m\ s^{-1}$, which translates to a planet mass of $M_b = 3.58 \pm 0.33\ M_\oplus$. With our homogeneously measured stellar radius and R_p/R_* from F. Dai et al. (2019), we measure an updated radius of $R_b = 1.47 \pm 0.03\ R_\oplus$. Combining our mass and radius measurements, we report a $CMF_b = 0.16 \pm 0.20$. This is consistent with the CMF suggested by its host star abundances (0.25 ± 0.03).

5.3. Kepler-407 b

Kepler-407 b is an $R_b = 1.161 \pm 0.039\ R_\oplus$ planet (L. M. Weiss et al. 2024) orbiting a G-type star on an ultra−short-period orbit of $P_b = 0.67$ days (P. Gajdoš et al. 2019). Additionally, this system hosts a nontransiting outer giant companion ($M_c \approx 11 M_J$) that sits on the boundary between giant planets and brown dwarfs with an orbital period of $P_c = 2096 \pm 5$ days (L. M. Weiss et al. 2024). Kepler-407 is one of the most metal-rich rocky planet hosts (0.35 ± 0.05; J. M. Brewer & D. A. Fischer 2018). In addition to being iron-rich, Kepler-407 is also rich in magnesium ($[Mg/H] = 0.32$ dex), with a ratio of [Fe/Mg] that would suggest an Earth-like $CMF_b = 0.31$ (J. M. Brewer & D. A. Fischer 2018).

This planet was confirmed with 17 RVs, but a precise mass measurement has proven very difficult to achieve (G. W. Marcy et al. 2014). L. M. Weiss et al. (2024) recently measured a mass of $M_b = 1.5 \pm 0.9\ M_\oplus$ using 70 HIRES RVs. To improve this mass measurement, we collected 10 RVs with HIRES and 13 with MAROON-X in 2021B, along with 13 RVs from KPF in 2023A.

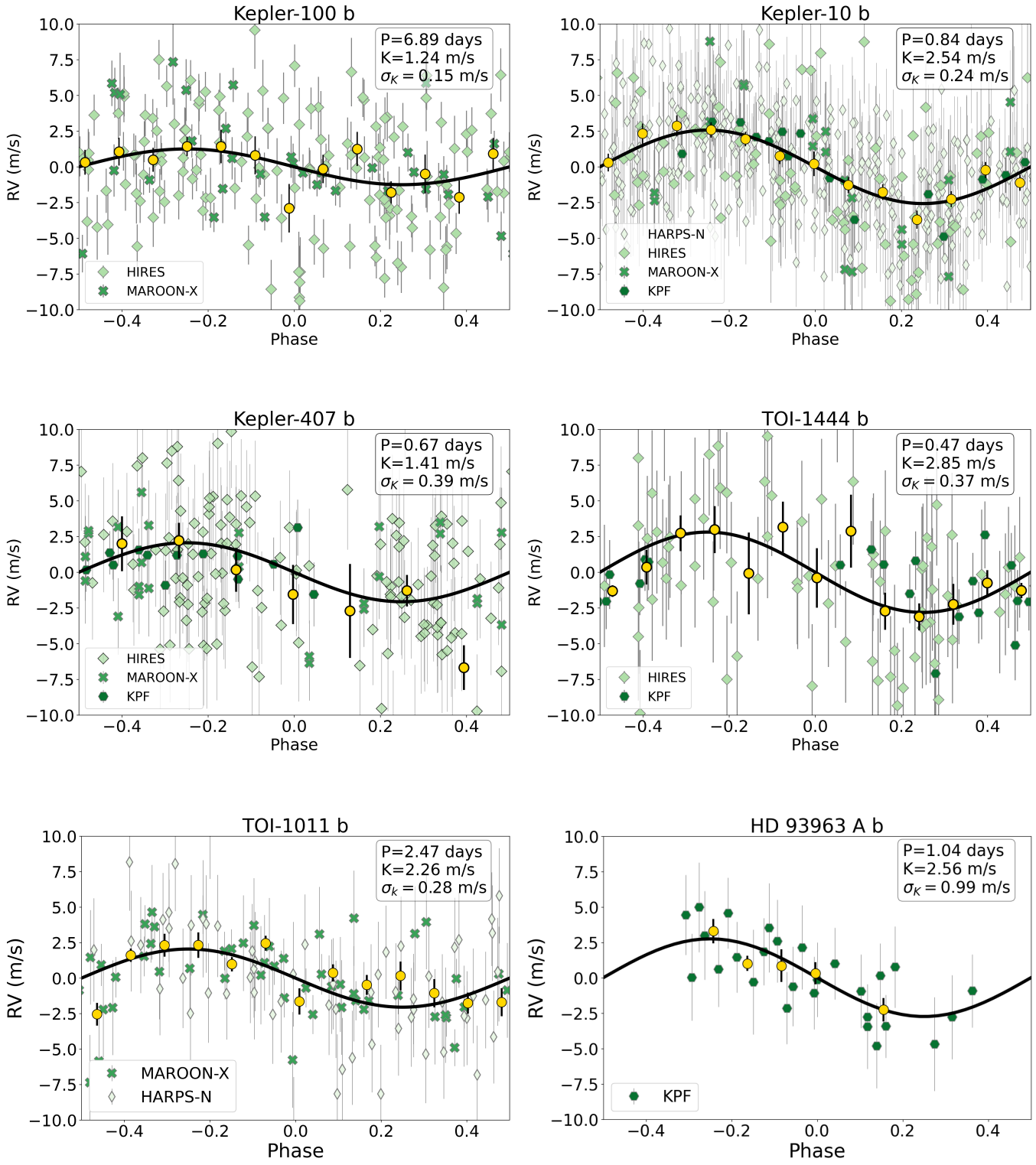

Figure 2. RVs phase folded at the period of each planet, after subtracting the RV components from the other three planets based on our best-fit model. The model RV curve for each planet is overplotted in gray, with the model period, semiamplitude (K), and standard deviation in semiamplitude (σ) shown. The gold points are the binned weighted median values with standard deviation of binned RVs as uncertainties.

We fit these RVs using a three-planet model and recover a best-fit semiamplitude of $K_b = 1.41 \pm 0.39\,\mathrm{m\,s^{-1}}$ (Figure 2). We get consistent solutions when fitting each RV set individually (HIRES: 1.63 ± 0.41; KPF: 1.72 ± 1.1; MAROON-X:1.3 ± 0.69). Using our best-fit K_b and our updated stellar mass, we recover a mass of $M_b = 1.93 \pm 0.50\ M_\oplus$.

With our homogeneously measured stellar radius and R_p/R_* from T. D. Morton et al. (2016), we measure an updated radius of $R_b = 1.19 \pm 0.05\ R_\oplus$. The mass and radius measurements for Kepler-407 b suggest an Earth-like composition of $\mathrm{CMF}_b = 0.35 \pm 0.32$, which is also consistent with that of its host star ($\mathrm{CMF}_* = 0.40$).

Table 3
Transit Parameters of TOI-1011 b

Parameter	Symbol	Prior	Posterior (Median and 68.3% CI)
Orbital period (days)	$P_{\rm orb}$	$\mathcal{N}$ (2.4697, 10)	2.470498 ± 0.000007
Time of conjunction (BJD −2,457,000)	T_c	$\mathcal{N}$ (2213.1309, 10)	1489.97760 ± 0.00383
Transit duration (hr)		$\mathcal{N}$ (2.3244, 10)	2.3016 ± 0.0341
Eccentricity	e	0 (fixed)	0
Impact parameter[†]	b	U (0, 1+$R_{\rm p}/R_\star$)	0.24 ± 0.15
Limb darkening q_1		U (0, 1)	0.55 ± 0.36
Limb darkening q_2		U (0, 1)	0.09 ± 0.35
Planet/star radius ratio	$R_p/R_\star$	$\mathcal{N}\propto$ transit depth	0.0143 ± 0.0006

5.4. TOI-1444

TOI-1444 is a solar-metallicity ([Fe/H] = 0.03) G-type star hosting an ultra−short-period (0.47 days) rocky planet with a radius of ∼1.4 $R_\oplus$. The rocky ultra-short-period planet has an outer, nontransiting companion with an $M\sin(i)$ consistent with a sub-Neptune-sized planet (F. Dai et al. 2021). Previously, F. Dai et al. (2021) measured a semiamplitude for the rocky USP of $K_b = 3.30 \pm 0.59$ m s^{-1} and a mass of 3.78 ± 0.71 $M_\oplus$. To measure a more precise mass, we obtained 18 RVs from KPF in 2023 August.

Using a two-planet model, we measure a best-fit semiamplitude of $K_b = 2.85 \pm 0.37$ m s^{-1} using both the HIRES and KPF data sets (Figure 2). Individually, the HIRES and KPF data sets produce values for K_b of 3.2 ± 0.4 m s^{-1} and 3.3 ± 0.4 m s^{-1}, respectively. This semiamplitude produces a planet mass of $M_b = 3.34 \pm 0.43$ $M_\oplus$. With our homogeneously measured stellar radius and R_p/R_* from A. S. Polanski et al. (2024), we measure an updated radius of $R_b = 1.42 \pm 0.04$ $R_\oplus$. These masses and radii give a CMF of $\mathrm{CMF}_b = 0.22 \pm 0.17$, which is consistent with an Earth-like composition and that of its host star ($\mathrm{CMF}_* = 0.29 \pm 0.03$) to within 1σ.

5.5. TOI-1011 b

The TESS mission (G. R. Ricker et al. 2015) collected 2-minute-cadence photometry of TOI-1011 (HD 61051, TIC 114018671) in sectors 34 and 61 (2021 January and 2023 January, respectively). TOI-1011 is a previously unconfirmed planet flagged in both SPOC and QLP pipelines in sector 34 photometry (D. A. Caldwell et al. 2020; M. Kunimoto et al. 2022). The parameters from these pipelines suggest an orbital period of $P = 2.4705 \pm 0.0000073$ days and a planet radius of $R_b = 1.45 \pm 0.11$ $R_\oplus$. We used Archival HARPS-N RVs (T. Trifonov et al. 2020) to identify a signal with a semiamplitude of $K_b = 2.4 \pm 0.8$ m s^{-1} for a single-planet model at the orbital period of the planet candidate.

To measure a precise mass for the planet, we obtained 40 RVs with MAROON-X in 2022A and 2023B. Using a single-planet model, we measure a best-fit semiamplitude of $K_b = 2.26 \pm 0.28$ m s^{-1}. Using the stellar mass measured in Section 4.4.1, we calculate a planet mass of $M_b = 4.59 \pm 0.56$ m s^{-1}. This confirms the planetary nature of the signal with a significance of 8σ.

The TESS data presented here were obtained from the Mikulski Archive for Space Telescopes (MAST) at the Space Telescope Science Institute. The specific observations analyzed can be accessed via doi: 10.17909/8zbx-8q79. To measure the planet radius, we used the Presearch Data Conditioning Simple Aperture Photometry (PDC-SAP) light curves (M. C. Stumpe et al. 2012, 2014) produced by the TESS Science Processing Operations Center (SPOC; J. M. Jenkins et al. 2016). We removed long-term variability and systematics from the light curves using an iterative sigma-clipping spline fit (using `wōtan`; M. Hippke et al. 2019). We first masked the transits according to the orbital period and time of inferior conjunction of TOI-1011 b from the SPOC pipeline on sector 34 photometry and then applied the detrending routine to the transit-masked light curves to ensure that the transit signal was not removed.

We employed `exoplanet` (D. Foreman-Mackey et al. 2021) and `pyMC3` (J. Salvatier et al. 2016) to construct the transit model for TOI-1011 b. Transit parameter priors (depth, duration, orbital period, and time of conjunction)[39] were adopted from the SPOC pipeline on sector 34 data, and stellar parameter priors (radius and density) were adopted from our isochrone fits. The priors (Table 3) were uniformly or normally distributed with large sigma values to allow for a thorough and unconstrained search of the parameter space. We supplied the stellar density prior to mitigate the degeneracy between the impact parameter b and scaled semimajor axis $a/R_\star$ of the planet. Limb-darkening coefficients q_1 and q_2 were adopted following the quadratic parameterization of D. M. Kipping (2013). The transit model further included the transit duration and the planet-to-star radius ratio $R_p/R_\star$, derived from the transit depth. We fit all the transits assuming a linear ephemeris, as we did not identify any significant TTVs. The initial constant-period maximum likelihood model served as an initial guess for posterior sampling. We then performed an MCMC analysis to sample the posterior distributions of the transit parameters. We find $R_{\rm p}/R_\star = 0.0143 \pm 0.0006$, which translates to a planet radius of $R_b = 1.45 \pm 0.05$ $R_\oplus$. The light curve phase folded at the period of TOI-1011 b is shown in Figure 3, while the corner plot showing our posterior distributions is shown in Figure 4.

Combining our radius and mass measurements, we compute a $\mathrm{CMF}_b = 0.33 \pm 0.26$. This suggests that TOI-1011 is a planet with an Earth-like composition.

5.6. HD 93963 A b

HD 93963 A b is a planet in an S-type orbit around a binary star, with an outer transiting Neptune-sized companion (HD 93963 A c). This rocky planet was previously reported to have a mass of $M_b = 7.8 \pm 3.2$ $M_\oplus$ and a radius of R_b 1.35 ± 0.04 $R_\oplus$, which would suggest an extremely iron-rich planet with a $\mathrm{CMF}_b > 1$ (L. M. Serrano et al. 2022). We collected 30 RVs

[39] We assumed a circular orbit ($e = 0$) in our transit fit similarly to our RV fit.

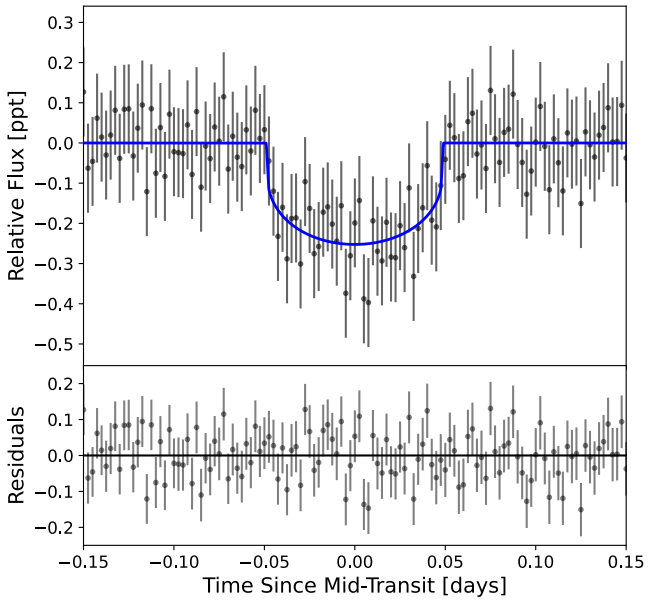

Figure 3. Phase-folded transit light curve of TOI-1011 b from sectors 34 and 61 of TESS photometry. We have binned the phased light curve (black) and show the best-fit transit model in blue. The bottom panel shows the binned residuals after removing the best-fit model.

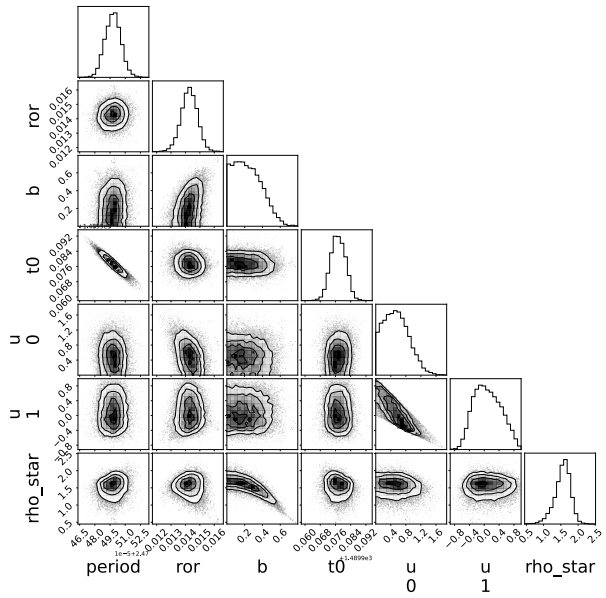

Figure 4. Corner plot of key transit model fit parameters for TOI-1011 b.

on HD 93963 A with KPF over nine nights from 2023 November to 2024 January.

We fit our full data set using a two-planet model and measured a best-fit semiamplitude of $K_b = 2.56 \pm 0.99$ m s^{-1} for the full data set (Figure 2). We get similar values using only the KPF RVs ($K_b = 2.62 \pm 1.3$ m s^{-1}). Using the stellar mass measured here, we calculate a planet mass of $M_b = 4.31 \pm 1.66\ M_\oplus$.

Recently A. S. Polanski et al. (2024) measured an updated value for R_p/R_* that is larger than the value from L. M. Serrano et al. (2022) by 2σ (0.0131 ± 0.0006, compared to 0.01190 ± 0.00036). We adopt the A. S. Polanski et al. (2024) value and use the stellar radius measured here to produce an updated radius of $R_b = 1.49 \pm 0.042\ R_\oplus$.

Combining our updated values for mass and radius, we calculate a CMF of $\mathrm{CMF}_b = 0.33 \pm 0.42$. The uncertainty on this mass measurement (and corresponding CMF) is large and is still therefore in agreement with a Mercury-like composition at the upper end of its 1σ posterior distribution. However, the median of the posterior suggests a composition more similar to that of Earth that is consistent with its host star ($\mathrm{CMF}_* = 0.31$).

6. Discussion

6.1. The Diversity of Rocky Planet Compositions

Figure 5 shows our newly measured masses and radii in comparison to the previous literature values in a mass–radius diagram. We see that for every planet (except TOI-561 b) the new mass measurement places the planet closer to an Earth-like composition (black solid line) than previously determined. Planets with a previous CMF smaller than Earth (Kepler-10 b and Kepler-407 b) now have a larger CMF after our analysis, while planets with a previous CMF larger than Earth (Kepler-100 b, HD 93963 A b, and TOI-1444 b) now appear to have a smaller CMF than previously determined. TOI-1011 b did not have a prior mass or radius measurement, but ours suggests that it has an Earth-like composition (CMF = 0.33).

We quantify this observation by computing the fractional rms error (RMSE) of our population of planets before and after our analysis against the Earth-like composition mass–radius model (L. Zeng et al. 2019). The fractional RMSE is the square root of the mean of squared fractional residuals:

$$\mathrm{RMSE} = \sqrt{\frac{1}{n}\sum_{i=1}^{n}\left(\frac{y_p - y_a}{y_p}\right)^2}, \tag{5}$$

where y_p is the predicted radius of a planet (at a given mass) with an Earth-like composition and y_a is the actual observed radius of the planet at a given mass. We find an RMSE of 0.14 (14%) for our planets using their initial mass measurements and an RMSE of 0.06 after our analysis. This supports the observation that the planets in our sample appear more "Earth-like" after updating their masses with precision RVs.

This is most apparent in the two high-density "super-Mercuries" in our sample (Kepler-100 b and HD 93963 A b); both had previous mass measurements that suggested a CMF close to 1.0 (or 100% iron). The updated mass measurements produce much lower CMFs of 0.53 for Kepler-100 b and 0.65 for HD 93963 A b. This supports studies finding that planets previously thought to be iron-rich super-Mercuries are becoming more Earth-like with additional high-precision RVs (R. Rodríguez Martínez et al. 2023; E. W. Guenther et al. 2024), Gaussian process modeling to account for stellar noise (C. L. Brinkman et al. 2023a), or updated stellar parameters (C. L. Brinkman et al. 2024).

6.2. Planet Host Star Connections

We now investigate the effect that these changes in planet composition—particularly our former super-Mercuries—have on the connection between planet and star compositions. Figure 6 shows our new planet CMFs as a function of host star [Fe/H] metallicity. We observe that planets orbiting low-metallicity stars tend to have small CMFs (TOI-561 b and Kepler-10 b), while planets orbiting high-metallicity stars have

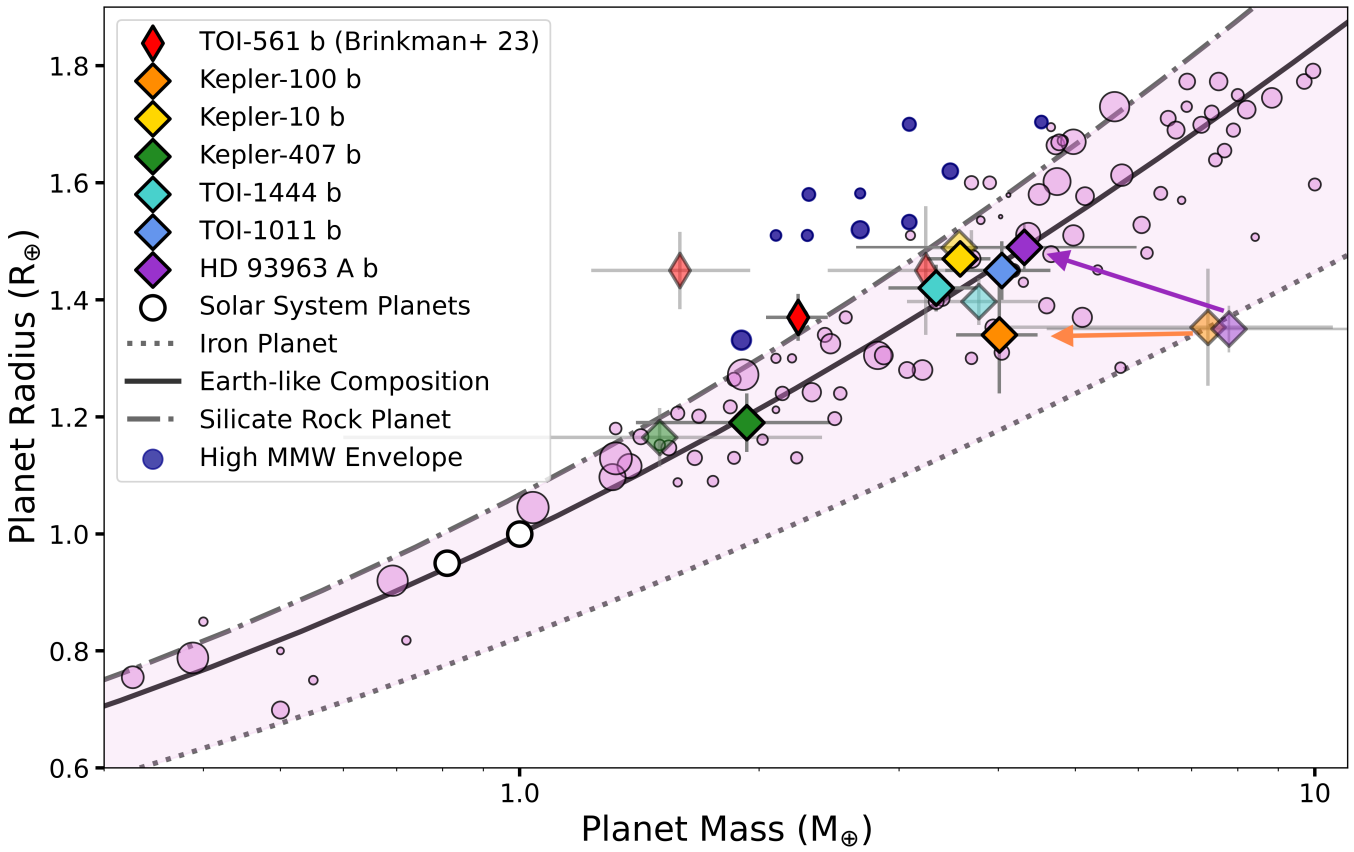

Figure 5. Planet radius vs. mass for our sample (diamonds) shown in the context of the rocky planet population (circles). Opaque diamonds represent our mass and radius measurements, while translucent diamonds are the previously published values. Lines show mass–radius relations for planets with an Earth-like composition, a purely silicate-rock composition, and a purely iron composition (L. Zeng et al. 2019). Literature values come from the NASA Exoplanet Archive (R. L. Akeson et al. 2013) queried 2024 April 12 for planets with mass and radius measurements with fractional uncertainties <50%, and the circle size is inversely correlated with fractional uncertainty in density. Planets consistent with a rocky composition (mixture of iron and silicate only) are shown in pink. Planets with masses and radii 1σ away from a pure silicate composition (dashed line) are shown in purple and possibly host envelopes made of high mean molecular weight (MMW) species.

a wider range in CMF, consistent with C. L. Brinkman et al. (2024). However, much of the visual trend seen in Figure 6 is driven by the low CMF of TOI-561 b, likely indicative of a high mean molecular weight gaseous envelope (G. Lacedelli et al. 2021; C. L. Brinkman et al. 2023b).

For five of the host stars in our sample (TOI-561, TOI-1444, Kepler-10, Kepler-100, and Kepler-407) we have [Mg/H] and [Fe/H] abundances (Kepler-407 from J. M. Brewer & D. A. Fischer 2018, the rest from C. L. Brinkman et al. 2024). The abundances for these stars are shown in Figure 7 against the broader population of exoplanet host stars. We also report [Fe/H] and [α/Fe] for TOI-1011. Two stars in our sample (TOI-561 and Kepler-10) have higher α abundances relative to iron that are characteristic of the chemically defined thick disk (B. E. Reddy et al. 2006; Figure 7), in agreement with previous findings (X. Dumusque et al. 2014; L. M. Weiss et al. 2021; C. L. Brinkman et al. 2024). Both TOI-561 b and Kepler-10 b have the smallest CMFs in our sample, which, along with the thick-disk planet HD 136352 b (CMF = 0.25, C. L. Brinkman et al. 2024), suggests that many rocky planets orbiting thick-disk stars could be iron-poor themselves.

We would expect smaller CMFs around thick-disk rocky worlds if they inherit the same ratio of iron to α abundances (such as Mg and Si) in their host star (C. Dorn et al. 2015). Beyond iron-to-silicate ratios, it has been suggested that the planetary building blocks of thick-disk stars should be more water-rich than those of the thin disk (N. Cabral et al. 2023), which could contribute to the formation of secondary water envelopes. This could further explain the existence of planets with small (and even negative) CMFs around thick-disk stars (such as TOI-561 b). However, the small sample size that plagues much of this analysis is very apparent here, and the discovery and characterization of additional rocky planets around thick-disk stars will illuminate whether they tend to be iron-poor or host gaseous envelopes of high mean molecular weight.

Figure 8 shows the updated CMF of these planets versus the equivalent CMF of their host stars (as described in Section 4.4.2). TOI-561 b is the only planet that deviates from the composition of its host star by $>1\sigma$, while the remaining four have a CMF consistent with their host stars. This is in agreement with the rocky planet sample in Figure 8, where 75% of planets have a CMF within 1σ of their host star. The density of TOI-561 b suggests that it is more iron-poor than its host star, but this is most likely due to the presence of a high mean molecular weight envelope and not reflective of the true planetary composition. The change in mass and therefore composition of Kepler-100 b and HD 93963 A b presented here brings both into agreement with the compositions suggested by their host star.

Previous studies have suggested not only a statistically significant relationship between planet and host star

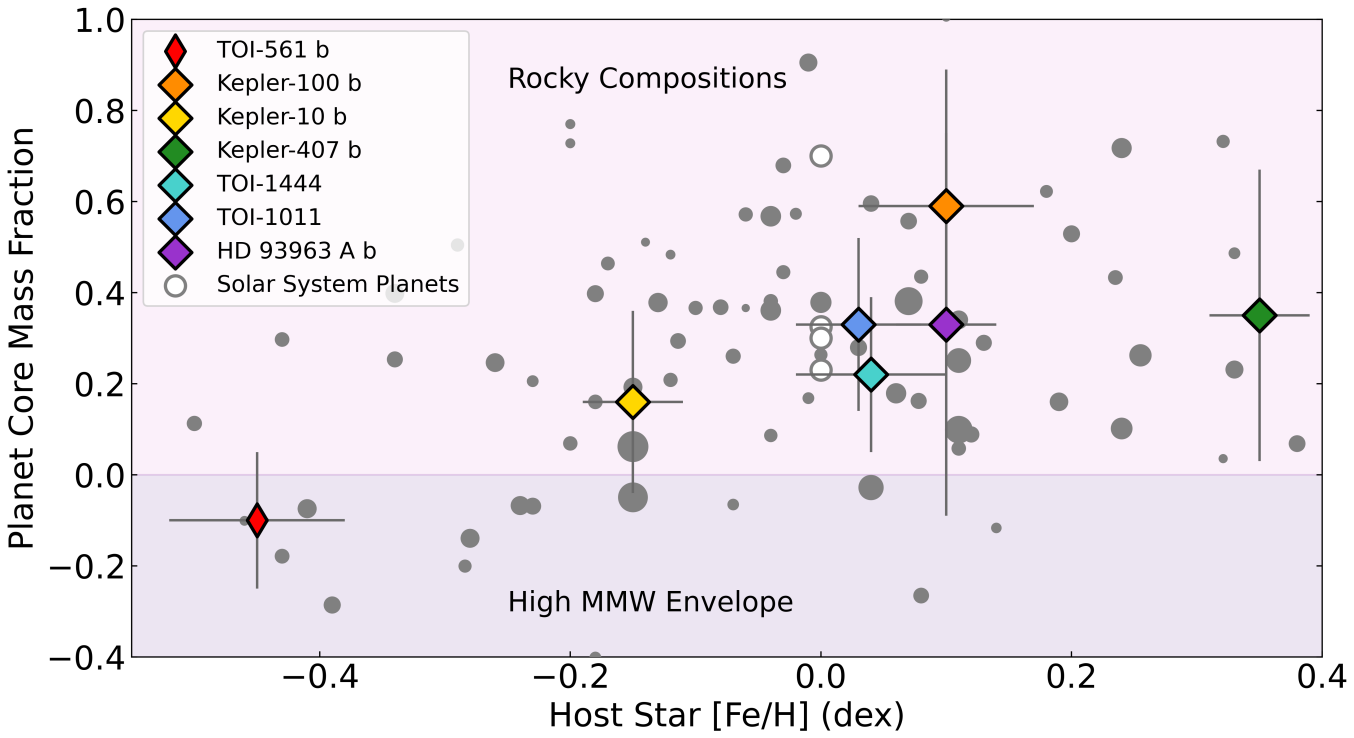

Figure 6. The CMF of rocky exoplanets vs. [Fe/H] metallicity for their host stars is shown for our sample in the context of the sample of rocky planets. The colors of each diamond correspond to the same planet as listed in Figure 5. The rocky planet point size is inversely correlated with fractional uncertainty in CMF.

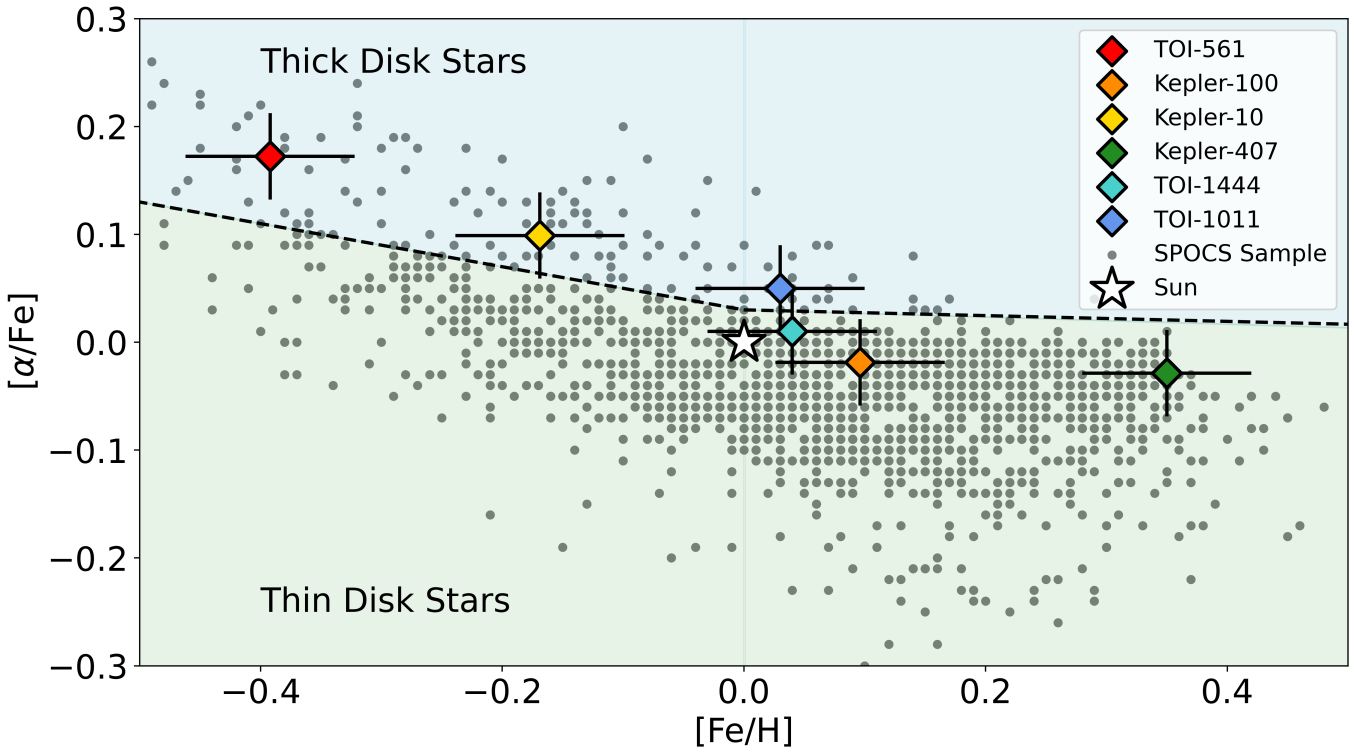

Figure 7. Alpha abundances [α/Fe] as a function of [Fe/H] for each host star in our sample, along with a larger sample of exoplanet hosts from the SPOCS catalog (J. M. Brewer & D. A. Fischer 2018). The colors of each diamond correspond to the same planet as listed in Figure 5. The black dashed line approximately separates the galactic thin-disk and thick-disk populations (L. M. Weiss et al. 2021). The two stars in our sample that fall above this line and were likely born in the galactic thick disk are labeled.

compositions but also a steep best-fit linear slope ($m = 5$–10; V. Adibekyan et al. 2021; Z. Liu & D. Ni 2023). A slope greater than $m = 1$ would imply that planets do not inherit the compositions of their host stars, but instead iron-rich stars preferentially produce planets enriched in iron relative to their primordial nebula, while iron-poor stars should host planets

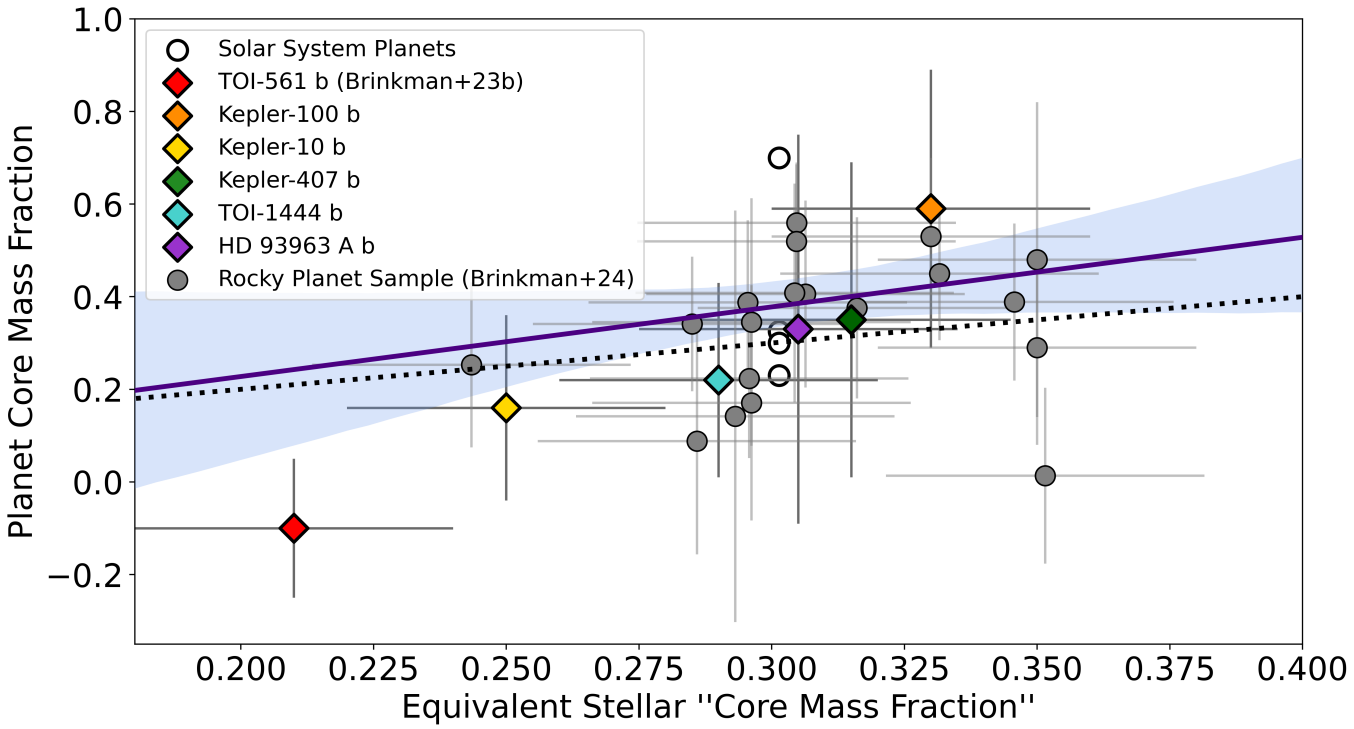

Figure 8. The CMF of rocky exoplanets vs. equivalent CMF for their host stars is shown for our sample in the context of the sample of rocky planets (from C. L. Brinkman et al. 2024). The CMFs for the four inner solar system planets are shown at the equivalent CMF of the Sun (from top to bottom: Mercury, Earth, Venus, and Mars). The dotted line shows the one-to-one correspondence of CMF in stars and planets, which is where planets would fall if they inherited the exact Fe/Mg ratio from their host star. Our linear best-fit model is shown in indigo (OLS with rejection sampling).

significantly depleted in iron. To test the effects that our updated planet compositions have on this linear slope, we perform a linear fit (form $y = mx + b$) where y is planet CMF, x is host star equivalent CMF, m is the slope, and b is the intercept. We use the `curve_fit` ordinary least-squares (OLS) functionality in `SciPy` to find the best-fit slope and intercept. We then use a Monte Carlo approach to estimate the uncertainties on these parameters by drawing values for CMF for each planet and star from Gaussian distributions and repeating the fit. As part of this process, we reject all values for planet density that produce a negative CMF (as this would no longer be a rocky planet) as to not bias our fit toward nonphysical values. We find a best-fit slope of $m = 1.3 \pm 1.0$ (indigo line in Figure 8). The fact that we measure a very shallow slope (consistent with $m = 1$) suggests that stars and planets have the same composition and is inconsistent with previous results. While C. L. Brinkman et al. (2024) also measured a slope much more shallow than previous studies, the updates in planet composition measured here produce an even shallower slope (easily compared in Table 4).

We perform two additional fits using orthogonal distance regression (ODR) to better to compare our results with previous studies (namely V. Adibekyan et al. 2021; Z. Liu & D. Ni 2023; C. L. Brinkman et al. 2024). We first perform this fit using the same sample of planets as above, which includes the negative CMF value for TOI-561 b, and recover a slope of $m = 3.9 \pm 1.1$. However, the negative value for CMF we report for TOI-561 b is not an accurate measurement of iron to rock for the planet and is simply an indication that it likely hosts a gaseous envelope. When we exclude TOI-561 b from the fit and only use planets with a positive CMF, our ODR fit produces a slope of $m = 2.6 \pm 1.2$. This slope is only 1σ larger than a slope of 1 and is smaller than that from V. Adibekyan et al. (2021), Z. Liu & D. Ni (2023), and C. L. Brinkman et al. (2024; Table 4). By updating planet parameters, namely mass, we find not only that the compositions of each planet appear to be more Earth-like but also that they seem to be closer reflections of the iron-to-magnesium ratio present in their host star.

Table 4
Comparison of Planet–Star Composition Relationships

Publication	Fitting Method	Slope
V. Adibekyan et al. (2021)	ODR	6.3 ± 1.2
Z. Liu & D. Ni (2023)	ODR	10.80 ± 3.56
(C. L. Brinkman et al. 2024)	ODR	5.6 ± 1.6
This work	ODR w/TOI-561 b	3.9 ± 1.1
This work	ODR w/o TOI-561 b	2.6 ± 1.2
This work (best fit)	OLS w/ Rejection Sampling	1.3 ± 1.0

7. Conclusions

We collected high-precision RVs on six planets using Keck/HIRES, Keck/KPF, and Gemini/MAROON-X, and we report updated mass and radius measurements for each planet here, including confirmation of the planet TOI-1011 b. We then calculated the CMFs and compared the compositions of planet to host star where possible. Our primary conclusions are as follows:

1. The CMFs of all planets in our sample become closer to that of Earth after updating their masses with precise

RVs. This suggests that most rocky planets on close-in orbits have compositions similar to Earth.
2. Two planets in our sample (Kepler-100 b and HD 93963 A b) had previous mass and radius measurements that suggested an extremely iron-rich CMF ≈ 1. The updated mass measurements for both planets shrink significantly and suggest compositions with smaller iron fractions (CMF of 0.53 and 0.65, respectively).
3. The one planet whose composition moved away from that of Earth is TOI-561 b, which appears to be in a class of super-Earth-sized planets hosting envelopes of high mean molecular weight.
4. Using only planets with positive CMF values, the relationship in the iron-to-magnesium ratios between stars and planets is consistent with being 1-to-1. This does not support previous conclusions stating a steep and statistically significant correlation between planet and host star compositions.
5. Planets orbiting α/Fe-enriched thick-disk stars have the smallest CMFs in our sample when compared to more metal-rich thin-disk stars. This suggests that these planets are potentially more likely to be iron-poor or host gaseous envelopes made of high mean molecular weight species.

The diversity of Earth-sized planets in many ways is less than it once appeared to be, with the reduction of planets belonging to the iron-rich "super-Mercury" population. However, planets such as TOI-561 b have radii less than 1.5 $R_\oplus$ yet likely host a gaseous envelope made of high mean molecular weight species (G. Lacedelli et al. 2021; C. L. Brinkman et al. 2023b; J. A. Patel et al. 2023). There are potentially many more planets historically grouped with "rocky planets" owing to their size, but which cannot have an accurate measurement of CMF owing to the presence of a high mean molecular weight envelope, such as GJ 3929 b, L 98-59 d, WASP-47 e, and 55 Cancri e (V. Bourrier et al. 2018; O. D. S. Demangeon et al. 2021; C. Beard et al. 2022; E. M. Bryant & D. Bayliss 2022; R. Hu et al. 2024). Phase-curve observations of many of these worlds with JWST would allow us to distinguish bare rocky planets from those with gaseous envelopes and demonstrate whether these planets are genuinely low in density or whether they, too, have an Earth-like interior composition.

Acknowledgments

The authors wish to recognize and acknowledge the very significant cultural role and reverence that the summit of Maunakea has always had within the Native Hawaiian community. We are most fortunate to have the opportunity to conduct observations from this mountain.

This work is based on observations obtained at the international Gemini Observatory, a program of NSF NOIRLab, which is managed by the Association of Universities for Research in Astronomy (AURA) under a cooperative agreement with the US National Science Foundation on behalf of the Gemini Observatory partnership: the US National Science Foundation (United States), National Research Council (Canada), Agencia Nacional de Investigación y Desarrollo (Chile), Ministerio de Ciencia, Tecnologìa e Innovación (Argentina), Ministério da Ciência, Tecnologia, Inovações e Comunicações (Brazil), and Korea Astronomy and Space Science Institute (Republic of Korea).

C.L.B. is supported by the National Science Foundation Graduate Research Fellowship under grant No. 1842402 and NASA's Interdisciplinary Consortia for Astrobiology Research (NNH19ZDA001N-ICAR) under award No. 19-ICAR19 2-0041.

L.M.W. acknowledges support from the NASA Exoplanet Research Program through grant 80NSSC23K0269.

D.H. also acknowledges support from the Alfred P. Sloan Foundation.

C.L.B. and L.M.W. also acknowledge support from NASA Keck Key Stragetic Mission Support grant No. 80NSSC19K1475.

N.S. acknowledges support by the National Science Foundation Graduate Research Fellowship Program under grant Nos. 1842402 and 2236415.

J.M.J.O. acknowledges support from NASA through the NASA Hubble Fellowship grant HST-HF2-51517.001, awarded by STScI. STScI is operated by the Association of Universities for Research in Astronomy, Incorporated, under NASA contract NAS5-26555.

This research was carried out, in part, at the Jet Propulsion Laboratory and the California Institute of Technology under a contract with the National Aeronautics and Space Administration and funded through the President's and Director's Research & Development Fund Program.

Facilities: TESS Keck:I, Gemini:Gillett.

Software: Radvel (B. J. Fulton et al. 2018), SuperEarth, (D. Valencia et al. 2006; M. Plotnykov & D. Valencia 2020), NumPy (C. R. Harris et al. 2020), Matplotlib (J. D. Hunter 2007), pandas (W. McKinney 2010), Astropy (Astropy Collaboration et al. 2013, 2018, 2022), SciPy (P. Virtanen et al. 2020).

ORCID iDs

Casey L. Brinkman https://orcid.org/0000-0002-4480-310X
Lauren M. Weiss https://orcid.org/0000-0002-3725-3058
Daniel Huber https://orcid.org/0000-0001-8832-4488
Rena A. Lee https://orcid.org/0000-0001-7058-4134
Gwyneth Tenn https://orcid.org/0009-0007-4721-9068
Jingwen Zhang https://orcid.org/0000-0002-2696-2406
Suchitra Narayanan https://orcid.org/0000-0002-0244-6650
Alex S. Polanski https://orcid.org/0000-0001-7047-8681
Fei Dai https://orcid.org/0000-0002-8958-0683
Jacob L. Bean https://orcid.org/0000-0003-4733-6532
Corey Beard https://orcid.org/0000-0001-7708-2364
Madison Brady https://orcid.org/0000-0003-2404-2427
Max Brodheim https://orcid.org/0009-0008-9808-0411
Ashley Chontos https://orcid.org/0000-0003-1125-2564
William Deich https://orcid.org/0009-0000-3624-1330
Jerry Edelstein https://orcid.org/0009-0002-2419-8819
Benjamin J. Fulton https://orcid.org/0000-0003-3504-5316
Steven Giacalone https://orcid.org/0000-0002-8965-3969
Steven R. Gibson https://orcid.org/0009-0004-4454-6053
Gregory J. Gilbert https://orcid.org/0000-0003-0742-1660
Samuel Halverson https://orcid.org/0000-0003-1312-9391
Luke Handley https://orcid.org/0000-0002-9305-5101
Grant M. Hill https://orcid.org/0000-0002-7648-9119
Rae Holcomb https://orcid.org/0000-0002-5034-9476
Bradford Holden https://orcid.org/0000-0002-6153-3076

Aaron Householder https://orcid.org/0000-0002-5812-3236
Andrew W. Howard https://orcid.org/0000-0001-8638-0320
Howard Isaacson https://orcid.org/0000-0002-0531-1073
Russ R. Laher https://orcid.org/0000-0003-2451-5482
Kyle Lanclos https://orcid.org/0009-0004-0592-1850
J. M. Joel Ong https://orcid.org/0000-0001-7664-648X
Joel Payne https://orcid.org/0009-0008-4293-0341
Erik A. Petigura https://orcid.org/0000-0003-0967-2893
Daria Pidhorodetska https://orcid.org/0000-0001-9771-7953
Claire Poppett https://orcid.org/0000-0003-0512-5489
Arpita Roy https://orcid.org/0000-0001-8127-5775
Ryan Rubenzahl https://orcid.org/0000-0003-3856-3143
Nicholas Saunders https://orcid.org/0000-0003-2657-3889
Christian Schwab https://orcid.org/0000-0002-4046-987X
Andreas Seifahrt https://orcid.org/0000-0003-4526-3747
Abby P. Shaum https://orcid.org/0000-0003-3133-6837
Martin M. Sirk https://orcid.org/0009-0007-8555-8060
Roger Smith https://orcid.org/0000-0001-7062-9726
Guðmundur Stefánsson https://orcid.org/0000-0001-7409-5688
Julian Stürmer https://orcid.org/0000-0002-4410-4712
Emma V. Turtelboom https://orcid.org/0000-0002-1845-2617
Dakotah Tyler https://orcid.org/0000-0003-0298-4667
Judah Van Zandt https://orcid.org/0000-0002-4290-6826
Josh Walawender https://orcid.org/0000-0002-6092-8295
Samuel W. Yee https://orcid.org/0000-0001-7961-3907
Sherry Yeh https://orcid.org/0000-0002-4037-3114

References

Adibekyan, V., Dorn, C., Sousa, S. G., et al. 2021, Sci, 374, 330
Agol, E., Dorn, C., Grimm, S. L., et al. 2021, PSJ, 2, 1
Akeson, R. L., Chen, X., Ciardi, D., et al. 2013, PASP, 125, 989
Angelo, I., & Hu, R. 2017, AJ, 154, 232
Asplund, M., Amarsi, A. M., & Grevesse, N. 2021, A&A, 653, A141
Astropy Collaboration, Price-Whelan, A. M., Lim, P. L., et al. 2022, ApJ, 935, 167
Astropy Collaboration, Price-Whelan, A. M., Sipőcz, B. M., et al. 2018, AJ, 156, 123
Astropy Collaboration, Robitaille, T. P., Tollerud, E. J., et al. 2013, A&A, 558, A33
Batalha, N. M., Borucki, W. J., Bryson, S. T., et al. 2011, ApJ, 729, 27
Bean, J., Seifahrt, A., Hartman, H., et al. 2010, Msngr, 140, 41
Beard, C., Robertson, P., Kanodia, S., et al. 2022, ApJ, 936, 55
Berger, T. A., Huber, D., Gaidos, E., & van Saders, J. L. 2018, ApJ, 866, 99
Bonomo, A. S., Dumusque, X., Massa, A., et al. 2023, A&A, 677, A33
Bonomo, A. S., Zeng, L., Damasso, M., et al. 2019, NatAs, 3, 416
Bourrier, V., Dumusque, X., Dorn, C., et al. 2018, A&A, 619, A1
Brewer, J. M., & Fischer, D. A. 2018, ApJS, 237, 38
Brinkman, C. L., Cadman, J., Weiss, L., et al. 2023a, AJ, 165, 74
Brinkman, C. L., Polanski, A. S., Huber, D., et al. 2024, AJ, 168, 281
Brinkman, C. L., Weiss, L. M., Dai, F., et al. 2023b, AJ, 165, 88
Bryant, E. M., & Bayliss, D. 2022, AJ, 163, 197
Cabral, N., Guilbert-Lepoutre, A., Bitsch, B., Lagarde, N., & Diakite, S. 2023, A&A, 673, A117
Caldwell, D. A., Tenenbaum, P., Twicken, J. D., et al. 2020, RNAAS, 4, 201
Choi, J., Dotter, A., Conroy, C., et al. 2016, ApJ, 823, 102
Ciardi, D. R., Fabrycky, D. C., Ford, E. B., et al. 2013, ApJ, 763, 41
Dai, F., Howard, A. W., Batalha, N. M., et al. 2021, AJ, 162, 62
Dai, F., Howard, A. W., Halverson, S., et al. 2024, AJ, 168, 101
Dai, F., Masuda, K., Winn, J. N., & Zeng, L. 2019, ApJ, 883, 79
Deck, K. M., Holman, M. J., Agol, E., et al. 2013, ApJL, 774, L15
Delrez, L., Ehrenreich, D., Alibert, Y., et al. 2021, NatAs, 5, 775
Demangeon, O. D. S., Zapatero Osorio, M. R., Alibert, Y., et al. 2021, A&A, 653, A41
Dorn, C., Khan, A., Heng, K., et al. 2015, A&A, 577, A83
Dressing, C. D., Charbonneau, D., Dumusque, X., et al. 2015, ApJ, 800, 135
Driscoll, P. E. 2018, in Handbook of Exoplanets, ed. H. J. Deeg & J. A. Belmonte, Vol. 76 (Berlin: Springer)
Dumusque, X., Bonomo, A. S., Haywood, R. D., et al. 2014, ApJ, 789, 154
Espinoza, N., Brahm, R., Henning, T., et al. 2020, MNRAS, 491, 2982
Foreman-Mackey, D., Hogg, D. W., Lang, D., & Goodman, J. 2013, PASP, 125, 306
Foreman-Mackey, D., Luger, R., Agol, E., et al. 2021, JOSS, 6, 3285
Fulton, B. J., Petigura, E. A., Blunt, S., & Sinukoff, E. 2018, PASP, 130, 044504
Fulton, B. J., Petigura, E. A., Howard, A. W., et al. 2017, AJ, 154, 109
Gajdoš, P., Vaňko, M., & Parimucha, Š. 2019, RAA, 19, 041
Gibson, S. R., Howard, A. W., Rider, K., et al. 2024, Proc. SPIE, 13096, 1309609
Gillon, M., Demory, B.-O., Van Grootel, V., et al. 2017, NatAs, 1, 0056
Guenther, E. W., Goffo, E., Sebastian, D., et al. 2024, MNRAS, 529, 141
Harris, C. R., Millman, K. J., van der Walt, S. J., et al. 2020, Natur, 585, 357
Hippke, M., David, T. J., Mulders, G. D., & Heller, R. 2019, AJ, 158, 143
Howard, A. W., Johnson, J. A., Marcy, G. W., et al. 2010, ApJ, 721, 1467
Howe, A. R., Burrows, A., & Verne, W. 2014, ApJ, 787, 173
Hu, R., Bello-Arufe, A., Zhang, M., et al. 2024, Natur, 630, 609
Huber, D., Zinn, J., Bojsen-Hansen, M., et al. 2017, ApJ, 844, 102
Hunter, J. D. 2007, CSE, 9, 90
Husser, T. O., Wende-von Berg, S., Dreizler, S., et al. 2013, A&A, 553, A6
Jenkins, J. M., Twicken, J. D., McCauliff, S., et al. 2016, Proc. SPIE, 9913, 99133E
Judkovsky, Y., Ofir, A., & Aharonson, O. 2022, AJ, 163, 91
Kipping, D. M. 2013, MNRAS, 435, 2152
Kite, E. S., & Schaefer, L. 2021, ApJL, 909, L22
Kopparapu, R. K., Wolf, E. T., & Meadows, V. S. 2020, in Planetary Astrobiology, ed. V. S. Meadows et al., Vol. 449 (Tucson, AZ: Univ. Arizona Press)
Kunimoto, M., Daylan, T., Guerrero, N., et al. 2022, ApJS, 259, 33
Lacedelli, G., Malavolta, L., Borsato, L., et al. 2021, MNRAS, 501, 4148
Liu, Z., & Ni, D. 2023, A&A, 674, A137
Lopez, E. D. 2017, MNRAS, 472, 245
Lopez, E. D., & Fortney, J. J. 2013, ApJ, 776, 2
Lovis, C., & Fischer, D. 2010, in Radial Velocity Techniques for Exoplanets, ed. S. Seager (Tucson, AZ: Univ. Arizona Press), 27
Marcy, G. W., & Butler, R. P. 1992, PASP, 104, 270
Marcy, G. W., Isaacson, H., Howard, A. W., et al. 2014, ApJS, 210, 20
McDonough, W. F., & Sun, S. 1995, ChGeo, 120, 223
McKinney, W. 2010, in Proc. 9th Python in Science Conf., ed. S. van der Walt & J. Millman (Austin, TX: SciPy), 56
Meadows, V. & NAI-Virtual Planetary Laboratory Team 2014, in Search for Life Beyond the Solar System. Exoplanets, Biosignatures & Instruments, ed. D. Apai & P. Gabor (Washington, DC: NASA), 2.1
Mills, S. M., Howard, A. W., Petigura, E. A., et al. 2019, AJ, 157, 198
Morton, T. D., Bryson, S. T., Coughlin, J. L., et al. 2016, ApJ, 822, 86
Owen, J. E., & Wu, Y. 2017, ApJ, 847, 29
Patel, J. A., Egger, J. A., Wilson, T. G., et al. 2023, A&A, 679, 17
Plotnykov, M., & Valencia, D. 2020, MNRAS, 499, 932
Polanski, A. S., Lubin, J., Beard, C., et al. 2024, ApJS, 272, 32
Rajpaul, V., Buchhave, L. A., & Aigrain, S. 2017, MNRAS, 471, L125
Reddy, B. E., Lambert, D. L., & Prieto, A. C. 2006, MNRAS, 367, 1329
Ricker, G. R., Winn, J. N., Vanderspek, R., et al. 2015, JATIS, 1, 014003
Rodríguez Martínez, R., Gaudi, B. S., Schulze, J. G., et al. 2023, AJ, 165, 97
Rogers, L. A. 2015, ApJ, 801, 41
Rogers, L. A., & Seager, S. 2010, ApJ, 712, 974
Rubenzahl, R. A., Halverson, S., Walawender, J., et al. 2023, PASP, 135, 125002
Salvatier, J., Wieckiâ, T. V., & Fonnesbeck, C., 2016 PyMC3: Python Probabilistic Programming framework, Astrophysics Source Code Library, ascl:1610.016
Schulze, J. G., Wang, J., Johnson, J. A., et al. 2021, PSJ, 2, 113
Scora, J., Valencia, D., Morbidelli, A., & Jacobson, S. 2020, MNRAS, 493, 4910
Seager, S., Kuchner, M., Hier-Majumder, C. A., & Militzer, B. 2007, ApJ, 669, 1279
Seifahrt, A., Bean, J. L., Stürmer, J., et al. 2016, Proc. SPIE, 9908, 990818
Seifahrt, A., Bean, J. L., Stürmer, J., et al. 2020, Proc. SPIE, 11447, 114471F
Seifahrt, A., Stürmer, J., Bean, J. L., & Schwab, C. 2018, Proc. SPIE, 10702, 107026D
Serrano, L. M., Gandolfi, D., Hoyer, S., et al. 2022, A&A, 667, A1
Soto, M. G., Anglada-Escudé, G., Dreizler, S., et al. 2021, A&A, 649, A144
Stumpe, M. C., Smith, J. C., Catanzarite, J. H., et al. 2014, PASP, 126, 100

Stumpe, M. C., Smith, J. C., Van Cleve, J. E., et al. 2012, PASP, 124, 985
Tayar, J., Claytor, Z. R., Huber, D., & van Saders, J. 2022, ApJ, 927, 31
Torres, G., Fischer, D. A., Sozzetti, A., et al. 2012, ApJ, 757, 161
Trifonov, T., Caballero, J. A., Morales, J. C., et al. 2021, Sci, 371, 1038
Trifonov, T., Tal-Or, L., Zechmeister, M., et al. 2020, A&A, 636, A74
Valencia, D., O'Connell, R. J., & Sasselov, D. 2006, Icar, 181, 545
Valencia, D., Sasselov, D. D., & O'Connell, R. J. 2007, ApJ, 656, 545
Van Eylen, V., Albrecht, S., Huang, X., et al. 2019, AJ, 157, 61
Virtanen, P., Gommers, R., Oliphant, T. E., et al. 2020, NatMe, 17, 261
Vogt, S. S., Allen, S. L., Bigelow, B. C., et al. 1994, Proc. SPIE, 2198, 362
Weiss, L. M., Dai, F., Huber, D., et al. 2021, AJ, 161, 56
Weiss, L. M., Isaacson, H., Howard, A. W., et al. 2024, ApJS, 270, 8
Weiss, L. M., & Marcy, G. W. 2014, ApJL, 783, L6
Weiss, L. M., Marcy, G. W., Petigura, E. A., et al. 2018, AJ, 155, 48
Weiss, L. M., Rogers, L. A., Isaacson, H. T., et al. 2016, ApJ, 819, 83
Winters, J. G., Cloutier, R., Medina, A. A., et al. 2022, AJ, 163, 168
Yee, S. W., Tamayo, D., Hadden, S., & Winn, J. N. 2021, AJ, 162, 55
Zechmeister, M., Reiners, A., Amado, P. J., et al. 2018, A&A, 609, A12
Zeng, L., Jacobsen, S. B., Sasselov, D. D., et al. 2019, PNAS, 116, 9723
Zeng, L., Sasselov, D. D., & Jacobsen, S. B. 2016, ApJ, 819, 127